Handbook of Heterogeneous Catalysis

8 Volumes

Volume 3

Edited by
Gerhard Ertl, Helmut Knözinger, Ferdi Schüth,
and Jens Weitkamp

Second, Completely Revised and Enlarged Edition

WILEY-VCH Verlag GmbH & Co. KGaA

4.5
Ultrathin Oxide Films

Hans-Joachim Freund and D. Wayne Goodman*

4.5.1
Introduction

Oxides play an important role in catalysis, both as supports for active materials as well as an active component itself [1]. Since the tools frequently used to study heterogeneous catalysts are limited in their ability to reveal details of oxide surface structure/properties, the atomic-level techniques of surface science offer numerous advantages as alternative investigative procedures, providing useful insights into the physics and chemistry

---

References see page 1333

* Corresponding author.

of oxide surfaces [2–6]. Applying the tools of surface science to the study of well-defined model catalysts has emerged and matured over the past two decades, and the surfaces of bulk single crystals as well as thin films have been investigated and the results extensively reviewed. In this chapter we concentrate on recent developments in the investigations of thin oxide films supported on metal single crystals. The material covered is organized as follows: first, a prototype system – namely the MgO(100) surface – is addressed, before discussing surfaces of other oxide materials. Included in this review is the interaction of these oxide surfaces with molecules from the gas phase, followed by the interaction of oxide surfaces with metal and metal oxide deposits, and how these composite systems interact with gas-phase reactants [7–20].

4.5.2 Magnesium Oxide

MgO(100) films have been prepared mainly on Mo(100) and Ag(100) substrates. Molybdenum has been chosen due to its high melting point as a refractory metal, and Ag on the other hand because it matches the lattice constant (2.9% mismatch as opposed to 6% for Mo(100)).

4.5.2.1 MgO(100)/Mo(100)

Epitaxial MgO(100) with thicknesses ranging from 2 to 100 monolayers (ML) can be grown by evaporating Mg onto Mo(100) at 300 K and 10^{-4} Pa (10^{-6} mbar) oxygen. Stoichiometric MgO(100) thin films have been characterized [21–31] using low-energy electron diffraction (LEED), Auger electron spectroscopy (AES), X-ray photoelectron spectroscopy (XPS), high-resolution electron energy loss spectroscopy (HREELS), electron energy loss spectroscopy (EELS), ultraviolet photoelectron and metastable impact electron spectroscopies (UPS/MIES), and temperature-programmed desorption (TPD). The films, while stable up to 1300 K, are reduced at higher temperatures by the Mo substrate, forming MoO_3 and Mg vapor. It has been shown, using XPS, EELS, UPS/MIES, and HREELS, that both the electronic and vibrational structures of thin MgO films are very similar to those of the bulk oxide; EELS and UPS/MIES have shown that these MgO films are almost free of point defects [32–38].

Surface sites may also be identified via adsorption and desorption of probe molecules such as CO. The interaction of CO with the MgO(100) surface is considered as a prototype system for studying properties of ionic surfaces, both from an experimental and a theoretical point of view [22, 39–48]. From the theoretical results it was concluded that CO binds weakly to regular terrace sites, with its carbon end down to surface Mg sites in an almost purely electrostatic manner [45].

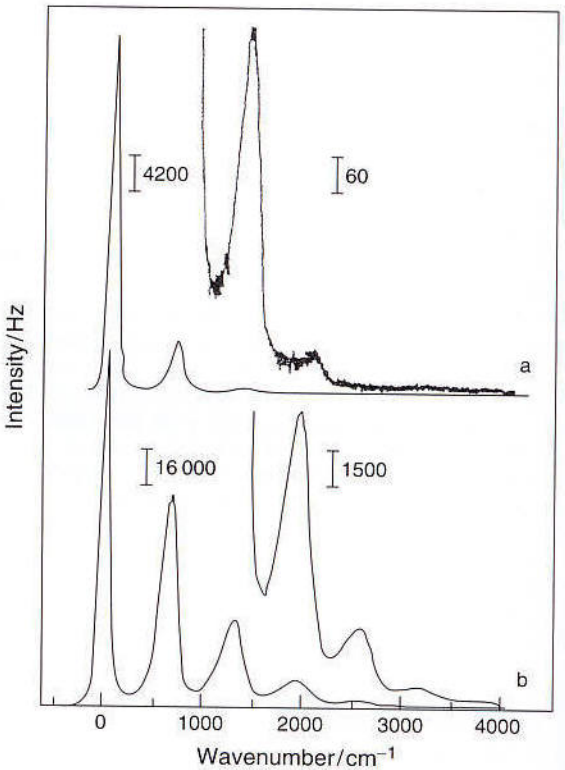

Fig. 1 High-resolution electron energy loss (EEL) spectra of MgO(100)/Mo(100): (a) $E = 46.2$ eV; (b) $E = 3.2$ eV.

Adsorption at low-coordinated sites – for example at steps, edges or corners – leads to an increase in the polarization of the molecule, and thus to a blue shift of the CO stretching frequency, and increasing binding energies as compared to CO adsorbed to regular terrace sites [22–25]. The magnitude of the CO binding energy has been controversially discussed [45]. However, CO-thermal desorption spectroscopy (TDS) data of vacuum-cleaved MgO single crystals resolved this discrepancy [42]. Very similar results were obtained for appropriately prepared MgO thin films [49]. Direct correlation of the TDS data with infrared (IR) data was possible, and allowed comparisons to be made to studies on microcrystalline samples. The acid–base properties of MgO(100)/Mo(100) have been characterized using HREELS and TPD [23, 24, 26]. Various probe molecules with increasing acid strength from alkanes and alkenes, to water and alcohols, to carboxylic acids were employed in these studies. The use of a high-energy electron beam (50 eV) and off-specular geometry allowed suppression of the strong surface optical phonons of substrate. As shown in Fig. 1, multiple phonon losses diminish as the electron beam energy increases. The HREELS results show that acetic acid, formic acid, methanol, and water undergo heterolytic dissociation, with the acidic proton adsorbed on the

basic oxygen anion sites and the conjugate base anions adsorbed on the cationic surface sites. Ethylene and ethane, however, are found to adsorb associatively on the MgO(100)/Mo(100) surface. Water and methanol each show a similar desorption behavior from the surface. A sharp peak near 150 K is attributed to condensation (of water or of methanol), while a broad peak near 300 K is probably associated with recombinative desorption.

High-quality TPD measurements of *n*-butane from MgO(100)/Mo(100) have been made for a large number of initial butane coverages (0–3.70 ML), and a wide range of heating ramp rates (0.3–10 K s^{-1}). The desorption energy was found to be 34.9 ± 3.4 kJ mol^{-1} at 0.5 ML. Simulations based on these results accurately reproduce TPD experiments for submonolayer initial coverages over a wide range of heating ramp rates (0.3–10 K s^{-1}). The desorption energy was found to increase with alkane chain length as $E_d(n) = 6.5 \pm 7.1 \times n$; that is, an increase of 7.1 ± 0.2 kJ mol^{-1} per CH_2 [50, 51].

The partial oxidation of methane to ethane on Li-promoted MgO(100)/Mo(100) has been studied by Wu et al. [27–29], using a combination of surface-science techniques and kinetic measurements at elevated pressures. The EELS spectra of MgO(100)/Mo(100) and Li/MgO/Mo(100), after annealing at different temperatures, are shown in Fig. 2. The peaks at 1.6, 3.6, and 5.33 eV have been attributed to the $[Li^+O^-]$ centers, F aggregates, and F centers, respectively. It has been found that the ethane formation rate correlates well with the F-center concentration, but not with the concentration of $[Li^+O^-]$ centers. The role of Li may be to promote F-center formation. These results indicate that $[Li^+O^-]$ centers are not likely to be involved directly in the methane activation step, but rather to promote the production of color centers in the near-surface region.

The interaction of metal atoms with MgO(100) may be regarded as a reference system for many other metal–oxide combinations. Single atom adsorption has been imaged for the case of Au [52]. At the lowest temperatures (8 K), Au adsorbs on terrace sites, but at higher temperatures (>30 K) the atoms diffuse to step and edge sites, as revealed through scanning probe microscopy (SPM) investigations (Fig. 3) [53]. The Au atoms reside on oxygen atoms in accord with theoretical predictions [53, 54]. The experimental proof comes from electron spin resonance (ESR) spectra through an analysis of the ^{197}Au hyperfine coupling on the single crystal thin film surface. It is interesting to note that the neutral Au atom (according to calculations, and in line with the experiments) is so strongly distorted in the 6s electron distribution that when CO is adsorbed on the Au atoms the CO becomes negatively charged, as indicated by a tilt of the CO–Au bonding axis, as the CO becomes isoelectronic with NO [55, 56]. In addition to single

References see page 1333

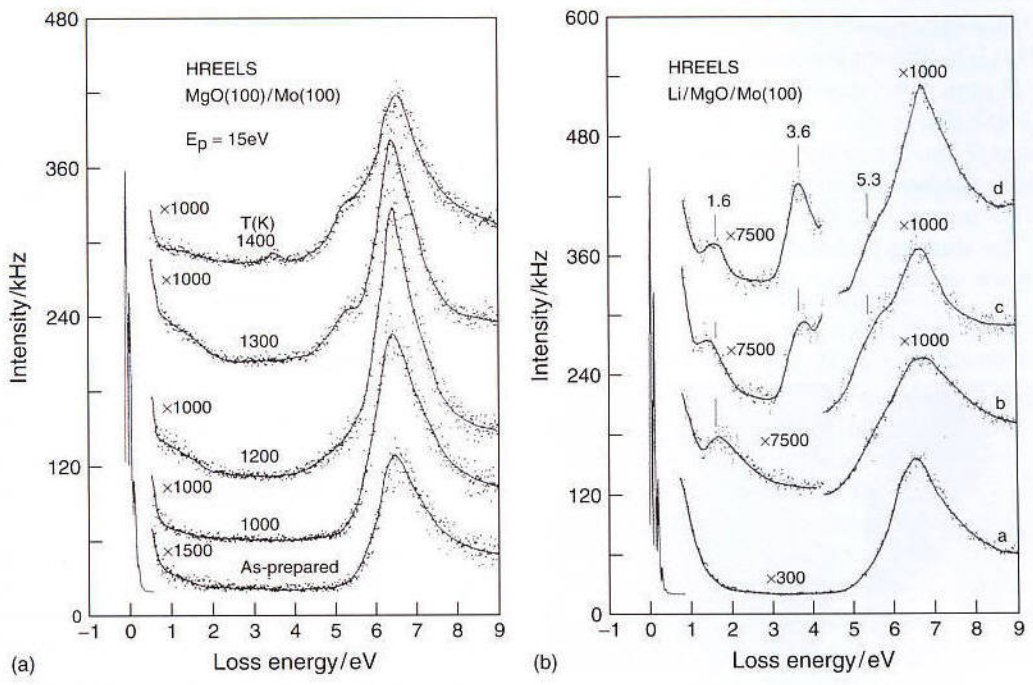

Fig. 2 High-resolution electron energy loss (EEL) spectra of: (left) MgO(100)/Mo(100); and (right) Li/MgO/Mo(100), taken after annealing to different temperatures.

neutral Au atoms, neutral Au clusters are also formed, depending on the amount of deposited metal. Neutral Au clusters exhibit a CO stretching frequency close to that of metallic Au. Partially, negatively charged Au atoms and small clusters may be produced by evaporating Au onto an electron-bombarded MgO(100) surface which contains paramagnetic charged and non-paramagnetic color centers [55].

Mass selected clusters in the gas phase have been deposited onto MgO(100)/Mo(100) surfaces and their reactivity investigated (see Refs. [57–60]). Figure 4 shows TDS measurements where CO has been oxidized to CO_2 as a function of Au cluster size [61]. There is a clear increase in reactivity at Au_8, and a marked decrease in reactivity with an increase in cluster size above Au_8. This trend has been explained by Au_8 clusters sitting on color centers. Presumably, the color centers are formed during thermal annealing pretreatments, as has been shown previously [28].

The heats of adsorption for metals (Cu, Ag, Pb) on MgO(100)/Mo(100) films have allowed the metal–MgO(100) adhesion energies to be calculated and the metal–MgO(100) bond energies to be estimated. The results suggest that local chemical bonds, both metal–oxygen and covalent metal–Mg, dominate the interfacial bonding for three-dimensional (3-D) films [62–71].

Molecular beams have been used directly to probe the desorption kinetics and dissociative sticking probability of methane on Pd nanoparticles supported on MgO(100)/Mo(100) compared with the corresponding values for Pd(111) [72]. Sticking measurements on supported Pd particles (3 nm), with the methane beam directed normal to the MgO(100) surface, results in a large fraction of the methane/Pd collisions occurring on regions of the particles where the beam direction is far from the local particle surface normal, and this causes a lower sticking probability. The sticking probability on 3-nm Pd particle is at most twice as large as on Pd(111). The TPD data of molecularly adsorbed methane show that Pd particles bind methane more strongly than does Pd(111) [72].

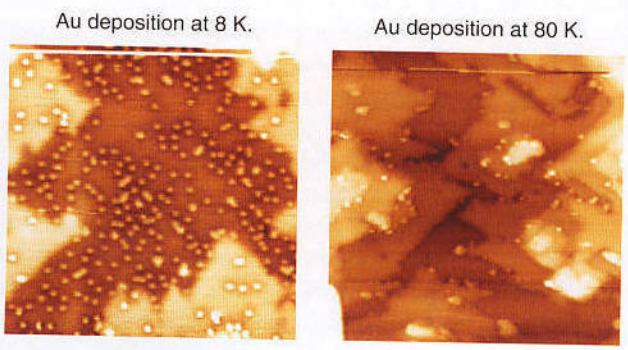

Fig. 3 Au atoms on MgO(001)/Ag(001) at 8 K (left panel) and 80 K (right panel).

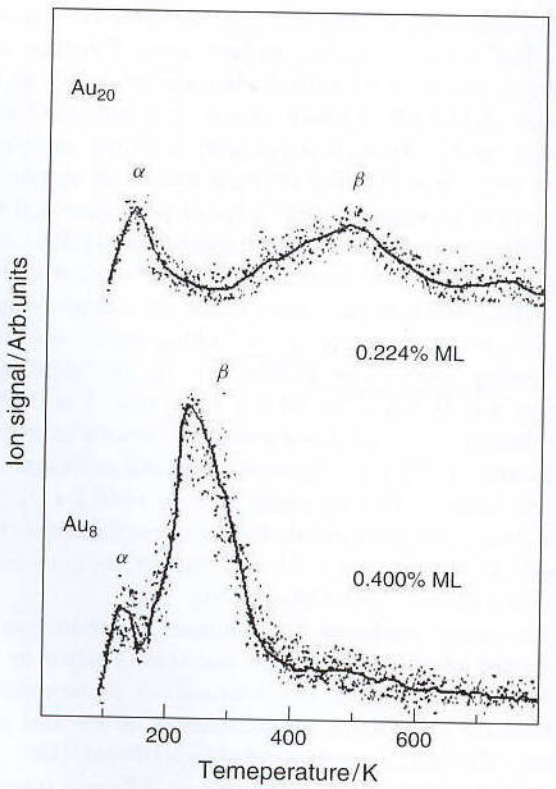

Fig. 4 Temperature-programmed reaction spectra for CO_2 production following CO and O_2 exposure at 90 K to Au_8 and Au_{20} Clusters an MgO [61].

There is an increasing number of reports on model studies of Au deposited on MgO [55, 56, 73, 74] and on other oxide films [75–77] to which we refer the reader at this point, and to which we return when we discuss SiO_2 films.

4.5.2.2 MgO(100)/Ag(100)

MgO(100)/Ag(100) systems may be prepared by evaporating metallic Mg from an alumina crucible in an oxygen background of 5×10^{-5} Pa at 350 K, followed by annealing to 500 K [78–83]. Figure 5 shows a LEED pattern together with the profile of the (0.0) spot and the deduced defect structure (represented schematically) included [78]. As in the case of MgO(100)/Mo(100) [39–41, 78–85], the as-prepared film appears to be free of point defects (color centers). By dosing electrons to the surface, color centers may be produced, as judged by EELS spectra in the electronic regime (Fig. 6) [86]. Exposure to oxygen quenches these defects and shows their location to be within the surface layer. Low-temperature scanning tunneling microscopy (STM) has been used to image the growth of

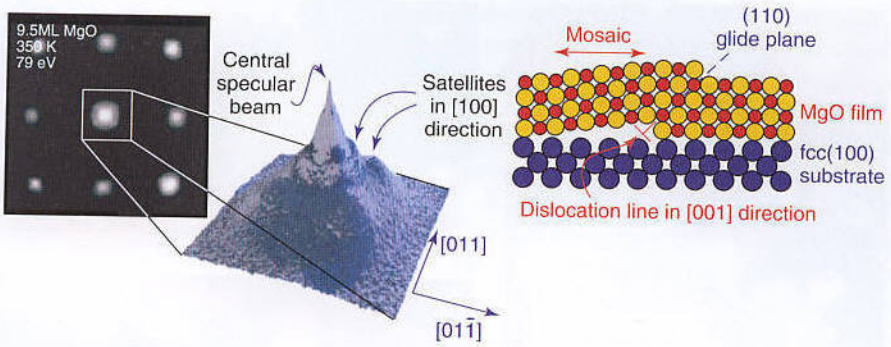

Fig. 5 The LEED pattern of a MgO film 9.5 ML thick, prepared at 350 K by evaporation of Mg in an oxygen atmosphere of 3×10^{-5} Pa. The fourfold streaky broadenings in the high-symmetry directions due to the misfit dislocations are clearly visible. The corresponding model is shown in the right-hand part of the figure [78].

the MgO(100) film on Ag(100) and the creation of color centers [80, 81, 84]. A series of images is shown in Fig. 7. The film exhibits line defects as revealed by the LEED profile analysis, but point defects only become visible by scanning tunneling spectroscopy (STS) after electron bombardment (Fig. 7c). After such a treatment, paramagnetic surface colors centers have also been detected by ESR spectroscopy under ultra-high vacuum (UHV) conditions [80]. The results can be compared directly with those from studies on powder samples [87–89].

4.5.2.3 MgO(111)/Mo(110)

The growth of epitaxial and stoichiometric MgO(111) thin films on a Mo(110) surface has been verified using LEED, XPS, AES, and ion scattering spectroscopy (ISS) [90, 91]. The MgO(111)/Mo(110) film is stable up to 1400 K, and is reduced by the Mo substrate at higher temperature, forming MoO_3 and Mg vapor. The adsorption of $[Re_2(CO)_{10}]$ and $[HRe(CO)_5]$ onto this thin film has been studied using TPD and IR absorption spectrometry (IRAS) [90, 91]. Both molecules decarbonylate on the surface, forming different surface-bound rhenium carbonyls, depending upon the surface temperature.

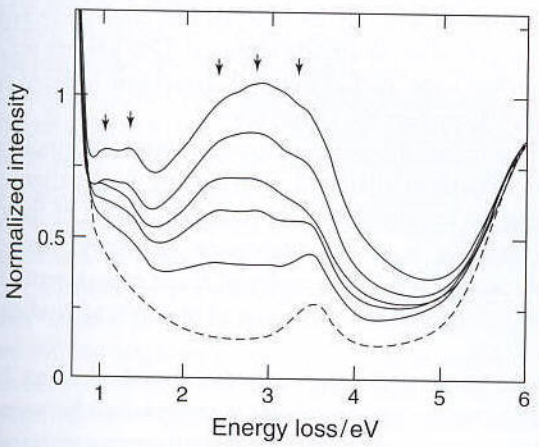

Fig. 6 Electron energy loss (EEL) spectra of 10 ML MgO on Ag(100) measured with a primary energy of 50 eV at room temperature, immediately after growth (lowest spectrum, dashed) and after electron bombardment with an incident energy of 200 eV. The exposure increases from bottom to top in the following steps: 140, 410, 540, 1260 up to 2160 electrons per surface oxygen ion. The five peaks at 1.0, 1.3, 2.4, 2.8, and 3.4 eV are marked by arrows [79].

4.5.3 Nickel Oxide

Stoichiometric NiO, a typical magnetic insulator which crystallizes in the rock salt structure, shows a band gap of 4.3 eV. Non-stoichiometric NiO can be either a *p*- or *n*-type semiconductor, depending on whether it has oxygen or nickel vacancies. Several low Miller-index faces have been prepared: NiO(100)/Ni(100), NiO(100)/Mo(100), and NiO(111)/Ni(111).

4.5.3.1 NiO(100)/Ni(100), Mo(100)

Because of the smaller lattice mismatch between NiO and Mo, as well as NiO and Al in comparison to NiO and Ni, the NiO(100)/Mo(100) is more highly ordered than NiO(100)/Ni(100). The NiO(100)/Ni(100) can be prepared by cycles of oxidation of Ni(100) with 1000 L of O_2 at 570 K, followed by annealing at 650 K, while NiO(100)/Mo(100) can be prepared by depositing Ni onto Mo(100) at an oxygen pressure of 10^4 Pa (10^{-6} mbar).

The NiO(100)/Ni(100) surface and its adsorption behaviors has been extensively characterized [92–99]. The electronic structure of NiO(100)/Ni(100) has been studied using XPS, angle- resolved ultraviolet photoelectron

References see page 1333

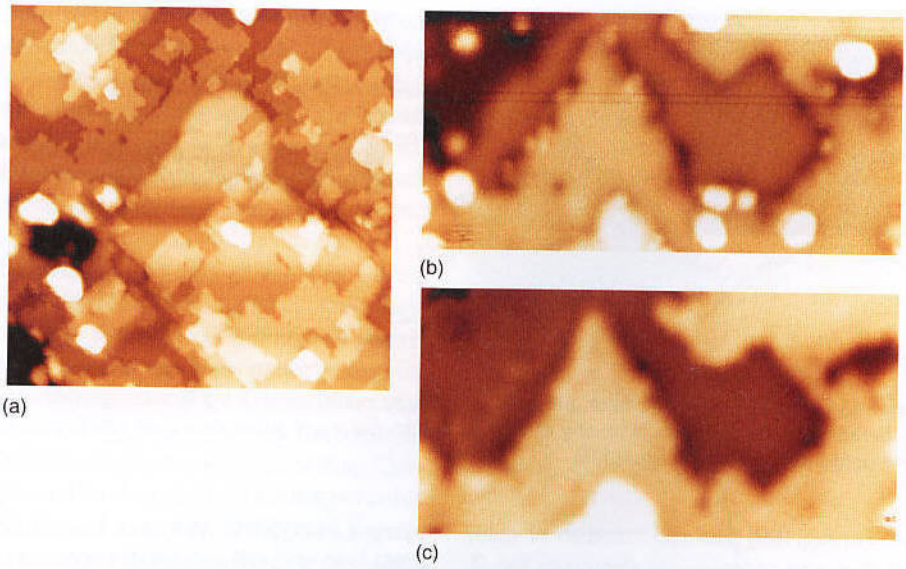

Fig. 7 Low-temperature (4 K) STM images (28×16 nm^2) of 4 ML MgO(001) = Ag(001). Panels (a) and (b) show the morphology of the MgO film as prepared, measured at $U_{bias} = +3.5$ V. Enhanced contrast for defects is obtained for $U_{bias} = -2.5$ V. (c) After electron bombardment as obtained with $U_{bias} = -2.5$ V [80].

spectroscopy (ARUPS), near edge X-ray adsorption fine structure (NEXAFS), HREELS, spot profile analysis-LEED (SPA-LEED), and *ab initio* calculations [92, 93, 100, 101]. These results have been compared with those obtained on an *in-vacuo*-cleaved NiO(100) single crystal. Both occupied states (ARUPS) and unoccupied states (NEXAFS) of the thin oxide film are very similar to those of the bulk oxide. On the basis of the ARUPS measurements, thin-film NiO(100)/Ni(100) and bulk NiO(100) also show very similar band structure, even along the direction perpendicular to the surface. The SPA-LEED and STM investigation by Bäumer and coworkers [94] showed that approximately 25% of the NiO(100)/Ni(100) film is covered by defects. One or two monolayer films show a behavior which is different from that of thicker films.

The adsorption of NO on NiO(100)/Ni(100) has been studied with TPD, XPS, HREELS, NEXAFS, and *ab initio* cluster calculations [92, 93]. Adsorbed NO has been found to be tilted by an angle of approximately 40° relative to the surface, with a binding energy of 0.52 eV. XPS measurements show strong satellites for N(1s), indicating significant screening, even on an insulating surface. Comparison of these results with TPD and XPS results for NO adsorption on an *in-vacuo*-cleaved NiO(100) single crystal shows that the adsorption behavior of NO, whether on thin oxide films or on the bulk oxide, is essentially identical. This result also indicates that the majority of NO is adsorbed on regular NiO sites rather than on defect sites. A proper theoretical description [102] of the bonding and structure of NO to NiO(100), as also revealed through photoelectron diffraction measurements by Woodruff et al. [103, 104], was only recently possible.

The influence of hydroxyl groups on the adsorption behavior of other small molecules on NiO(100)/Ni(100) has been studied by Cappus et al. [98], using TPD, EELS, ARUPS, and XPS. It was found that OH adsorbs only on defect sites, consistent with the fact that no hydroxyl group formation has been found on a cleaved NiO(100) single crystal surface, which has only a very limited amount of defect sites. Both dehydroxylated and hydroxylated NiO surfaces show almost identical TPD spectra for NO, consistent with the fact that NO adsorbs on ordered sites, while OH prefers the defect sites.

Photoinduced desorption experiments of NO molecules from NiO(100)/Ni(100) films, resolving the distribution of energy on translational and internal degrees of freedom and relating it to the adsorption geometry, have also been carried out. The results of these experiments have been interpreted on the basis of theoretical studies [95, 105–112].

NiO(100)/Ni(100) have also been studied using EELS and *ab initio* calculations [98]. A comparison between the EELS spectrum of the clean NiO(100) surface with spectra of the OH-contaminated and the NO-covered surface is provided in Fig. 8. The two peaks at 0.57 and 1.62 eV are very sensitive to NO adsorption, but not to OH adsorption, indicating that they are due to surface states, and that these surface states are located at regular NiO surface sites. On the basis of *ab initio* calculations, these surface states were attributed to a d–d transition of the nickel

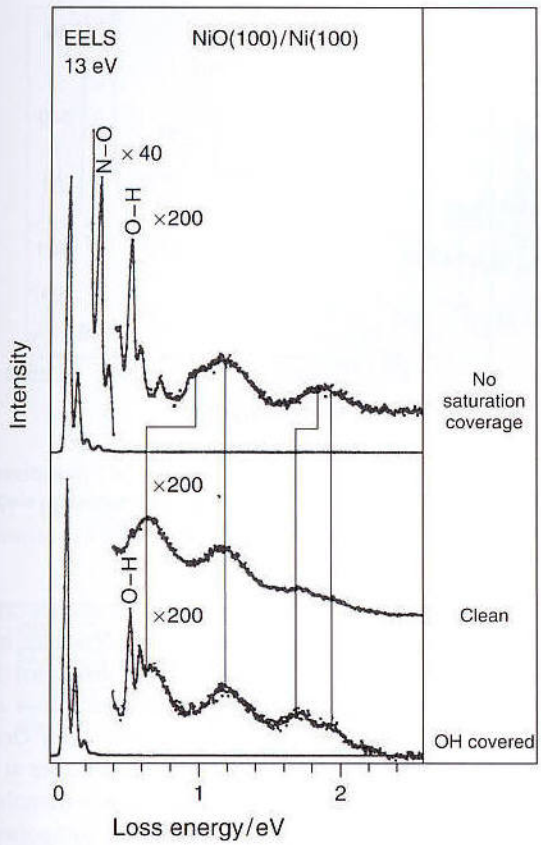

Fig. 8 Electron energy loss (EEL) spectra of clean NiO(100)/Ni(100) and adsorbate-covered surface. (Adapted from Ref. [97], with permission.)

surface ions [97]. These states have been identified as ^3E (0.59 eV), $^3A_2$ or ^3E, or a superposition of both (1.62 eV).

The adsorption of formic acid, ammonia, formaldehyde, and alcohols on NiO(100)/Mo(100) has been studied using TPD and HREELS [113–116]. Formic acid [113] adsorbs associatively at 90 K and undergoes heterolytic dissociation upon heating to above 200 K to produce a formate intermediate. The adsorbed formate species is proposed to bond to a Ni cation site via one of the oxygen atoms of the formate in a monodentate configuration. Upon further heating, formic acid desorbs from the surface between 300 and 400 K via recombination of surface formate and surface hydrogen. Methanol and ethanol [116] adsorb associatively at 90 K and desorb reversibly upon heating. Both alcohols are bonded to the Ni cation sites via their oxygen atom with the methyl or ethyl group directed away from the surface. No γ(OH) loss feature has been observed in HREELS, indicating the formation of strong hydrogen bonds between the hydroxyl hydrogen and the lattice oxygen. It has been proposed that the hydroxyl proton of each alcohol fluctuates about the neighboring oxygen anion sites, acting as a mobile proton. Formaldehyde [115] adsorbs molecularly and desorbs upon heating to 350 K; extensive polymerization of formaldehyde has been observed. Monomeric formaldehyde is chemisorbed onto Ni cationic sites in the oxygen end-on η^1(O) orientation, leading to a shift of the γ(CO) feature to 1650^{-1} cm. A η^2(C, O) form of adsorbed formaldehyde is indicated by a γ(CO) loss feature at 1320^{-1} cm in HREELS. Ammonia adsorbs molecularly [117] via the nitrogen lone pair onto the Ni caution site. The HREELS data show that the umbrella mode of ammonia exhibits great charge sensitivity, and that the frequency of this mode remains unchanged as a function of NH_3 exposure. Accordingly, the frequency of the umbrella mode can be utilized as a fingerprint for the nature of the cations of oxide materials, independent of the ammonia adsorption geometry and coverage.

The interaction of CO with NiO(100)/Mo(100) has also been investigated with IRAS [118]. Using isobars constructed from measurements in a pressure range of 10^{-6} to 10^2 Pa (1×10^{-8} to 1 mbar), and over a temperature range of 93 to 280 K, the isosteric heat of CO adsorption has been determined as approximately 10.4 kcal mol^{-1}, with the heat of adsorption decreasing slightly with increasing CO coverage.

4.5.3.2 NiO(111)/Ni(111)

The adsorption of hydroxyls on NiO(111)/Ni(111) has been studied using EELS, XPS, ARUPS, and isotope exchange experiments [98]. In contrast to the NiO(100)/Ni(111) surface, the hydroxyl group has been found to be bound on the regular site of the (111) surface [98, 99, 119, 120]. This difference has been attributed to the instability of the polar surface.

If a hydroxyl-terminated NiO(111)/Ni(111) surface is heated, at around 500 K water desorbs and a rather disordered c(2 × 2) LEED pattern can be observed. This LEED pattern is related to the so-called octopolar reconstruction of the clean NiO(111) surface, which leads to a stable surface and has also been observed later for NiO bulk systems. If properly treated with water, the reconstructed surfaces can also be retransformed into the hydroxylated surface.

The adsorption of NO on the hydroxylated and dehydroxylated NiO(111)/Ni(111) surface shows very different TPD behavior [121]. From the TPD area it has been estimated that almost two-thirds of the surface area is blocked by OH. Domen and coworkers investigated the adsorption of CO (and in particular formic acid) on this system using IRAS and sum frequency generation (SFG). These authors identified intermediates of formic acid bonding and its reaction partly using time-resolved studies [122–125].

References see page 1333

There are also reports on other rock salt oxide thin film systems, such as CoO(111)/CO(0001), as well as FeO(111)/Pt(111) ([307, 310] see below), but for details of these studies the reader is referred to the literature [121, 126–129, 307, 310].

4.5.4 Alumina

Aluminum oxide is a widely used support for heterogeneous catalysts. While aluminum oxide may crystallize in various structures depending on conditions and precursors used in its preparation, α-alumina is thermodynamically the most stable structure over a wide temperature range.

4.5.4.1 Alumina/NiAl(110)

A thin, very well-ordered alumina film may be grown on NiAl(110) [130, 131]. Both other low-index terminations of NiAl (i.e., NiAl(111)) as well as NiAl(100) lead to oxide films that are not morphologically conform [6, 132, 133]. However, very uniform films may be grown on $Ni_3Al(111)$ [134–136]. Epitaxial aluminum oxide grown on NiAl(110) has been studied using LEED, ELS, HREELS, XPS, ARUPS, and STM [12, 137, 138].

Density functional calculations succeeded in modeling the structure which is shown in Fig. 9 [139]. The model reproduces all available experimental data, including the very detailed phonon spectrum of the material (Fig. 10). The material is characterized at the top by an almost coplanar Al–O layer, as it is predicted also for alumina surfaces terminating bulk single crystal. Its structure is characterized by Al ions in different coordinative environments, and may be compared with a structure which is believed to exist on an oxygen-deficient corundum surface. The oxide layer contains domain boundaries, both regular domain as well as antiphase-domain, which turn out to play an important role in the reactivity of the film towards molecules and metal deposits. The stoichiometry of the film is $Al_{10}O_{13}$. It is an oxygen-deficient alumina.

The band structure along two azimuths (110, 100) has been determined and compared to calculations, as shown in Fig. 11 [130].

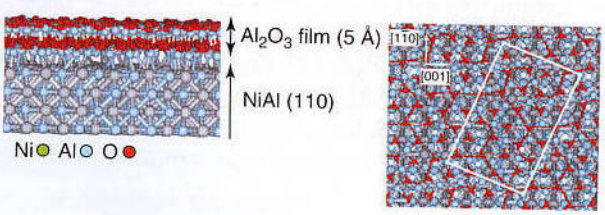

Fig. 9 The structure of alumina/NiAl (110) [139].

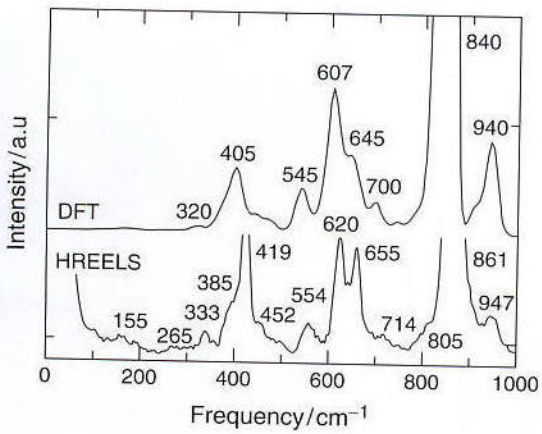

Fig. 10 Infrared-active modes as calculated by DFT (broadened by a Gaussian with a width of 20 cm^{-1}) and high-resolution electron energy-loss spectrum (HREELS). (From Ref. [342].)

Most molecules interact with the alumina surface rather weakly. The adsorption of CO on alumina has been studied with EELS (Fig. 12) [140]. The vibrational fine structure of the energy loss peaks due to the $^1\Sigma^+ \rightarrow a^3\Pi$ electronic transition of adsorbed CO has been clearly resolved for the first time for adsorbed molecules at the (sub)monolayer level. The EELS results for one monolayer show larger line widths for the vibrational components, and a higher excitation energy than for the multilayer. The half-widths of the loss peaks have been used to estimate the lifetime of the excited states.

NO, on the other hand, interacts with the film by forming compounds such as nitrites and nitrates at higher exposures and room temperatures [141]. The reaction appears to occur exclusively at the domain boundaries in the film, as this reactivity may be completely suppressed by selective decoration of the defect by Pd metal deposition [142].

Pt clusters supported on alumina and CO adsorption on the supported clusters have been characterized using STM, SPALEED, ARUPS, HREELS, EELS, TPD, XPS, and TEM [9, 120, 143–147]. The results showed that the oxide film is strongly modified by deposition of Pt onto the alumina surface, and that Pt is incorporated into the oxide layer. In addition to CO desorption from metallic Pt, a low-temperature CO desorption state has been found which was attributed to Al_2O_3 [148] modified by Pt. HREELS results show that CO is adsorbed on the top site at small and intermediate CO coverages, while at higher CO coverages the bridge site is also populated. XPS results at 300 K show a peak at 284.8 eV, typical for adsorbed carbon, in addition to a peak corresponding to molecularly adsorbed CO. These results indicate that dissociative CO adsorption occurs on small Pt clusters even at room temperature.

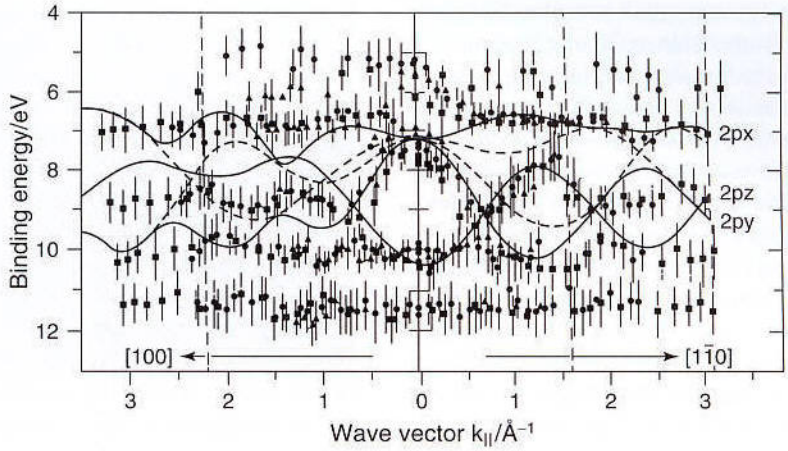

Fig. 11 Band structure of γ-Al_2O_3(111)/NiAl(110) measured by ARUPS. The solid line is the result of a tight binding band structure calculation of a 2-D O^{2-} overlayer. (Adapted from Ref. [130].)

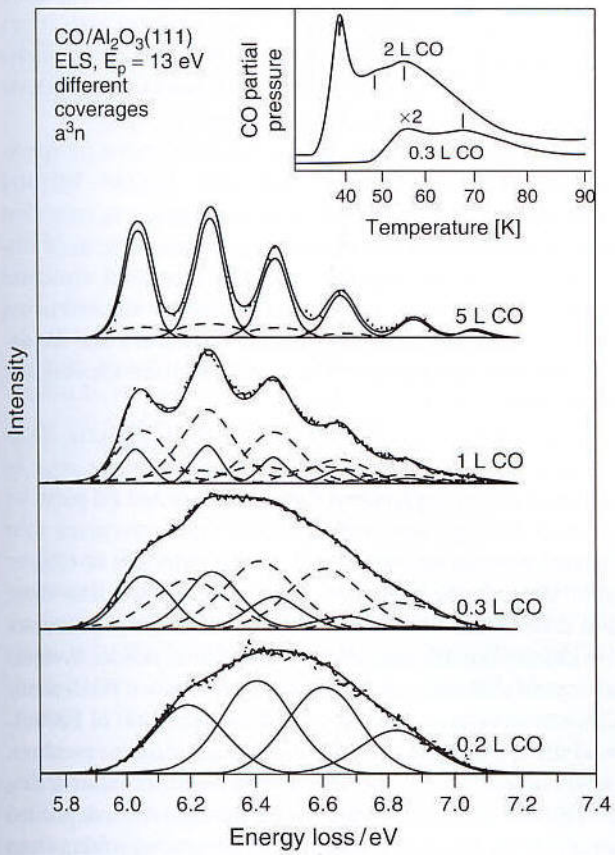

Fig. 12 Electron energy loss (EEL) spectra of CO on γ-Al_2O_3(111)/$NiAlO_3$(110) at different CO coverages. (Adapted from Ref. [140].)

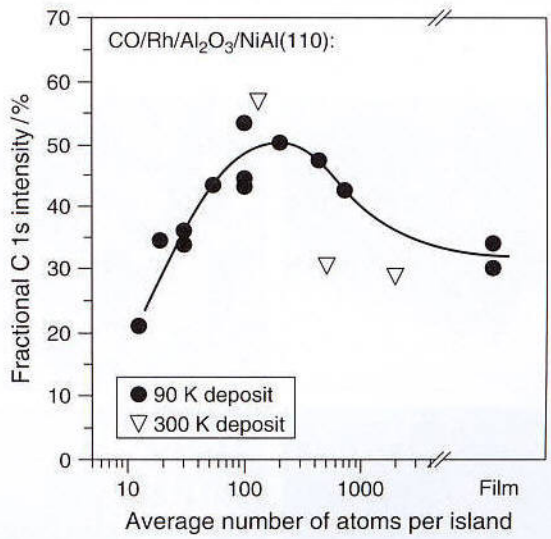

Fig. 13 CO dissociation activity on alumina-supported Rh particles as determined by XPS. Note that the behavior of the particles grown at 300 K (triangles) is not fully identical to the behavior of 90 K deposits (circles) [155, 156].

Rhodium has been deposited on the same alumina films using the control of the growth conditions to prepare Rh particle distribution with different average particle sizes [149]. The size distributions have been characterized with STM [9, 150]. It is known from metal single-crystal studies that CO adsorbs and desorbs molecularly on clean low-index Rh surfaces [151]. On the other hand, conflicting evidence has been reported from the catalytic literature for the onset of CO dissociation as a function of particle size [152–154]. Some authors claim that CO dissociation probably increases with increasing particle size, while others report the opposite effect. Figure 13 shows the CO dissociation probability as a function of particle size for Rh deposits on alumina films [155, 156]. The dissociation

References see page 1333

most likely goes to zero for very small particles, in agreement with expectations from stable molecular Rh carbonyl complexes, but it decreases for large particles, asymmetrically reaching a value similar to stepped Rh single crystal surfaces [157, 158]. In an intermediate regime the dissociation goes through a maximum correlating with the formation of rough particles, as indicated by their aspect ratio. This result allows one to explain the observation of decreasing or increasing CO dissociation probability on real powder catalysts, if the exact average particle size is not well known.

Much data have been accumulated for Pd deposition on the alumina film [12, 16, 19, 159]. Figure 14 shows STM images of particles of 6 nm average size with well-resolved facets [160], although smaller particles, down to a size containing only a few atoms, have also been studied. Single Pd atoms have been imaged on the alumina film [161]. Bimetallic alloy particles (Pd–Co and Pd–Ag) have also been prepared, characterized and studied with respect to reactivity [162–167].

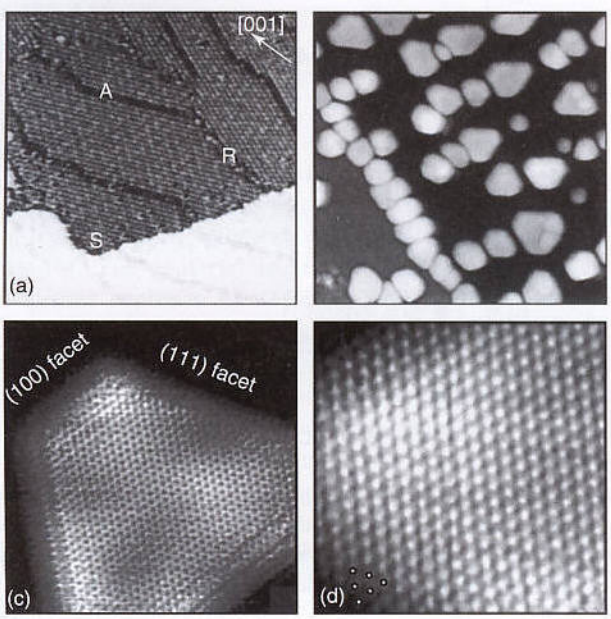

Fig. 14 (a) A STM image (500 × 500 Å^2) of the aluminum oxide film formed on NiAl(110) by oxidation. A step edge (S), a reflection domain boundary (R), as well as an antiphase domain boundary (A) are indicated. Tunnel current $I_t = -0.4$ nA, sample bias $V_s = -1.3$ V. (b) A 650 × 650 Å^2 image recorded after deposition of ≈2 ML of Pd at room temperature. Palladium clusters have nucleated preferentially at a step and at domain boundaries. Both crystalline and less-ordered clusters are seen. $I_t = -1.0$ nA, $V_s = -0.9$ V. Atomic-resolution images of crystalline nanosize Pd clusters. (c) 95 × 95 Å^2, $I_t = -0.8$ nA, $V_s = -5.0$ mV. (d) 45 × 45 Å^2. The resolution is kept a few layers down the sides, allowing identification of the side facets. The dots indicate atomic positions consistent with a (111) facet. $I_t = -1.8$ nA, $V_s = -1.5$ mV [160].

The adsorption and reaction of a variety of molecules has been studied in detail, both under typical UHV-conditions, in a molecular beam [19], and at elevated pressures [168–179]. The most frequently studied molecules are CO, NO, CH_3OH and C_2H_4 involved in oxidation, hydrogenation and oxidation dehydrogenation reactions. Under no circumstances had CO dissociation been observed for Pd/alumina [180] model systems [181], while on real systems such observation has been reported [182, 183]. However, CO bond cleavage has been seen for CH_3OH dehydrogenation on Pd/alumina [180]. Here, detailed molecular beam experiments showed that the cleavage occurs before the methanol molecule has been fully dehydrogenated. The reaction happens very rapidly at the edges and corner of the Pd nanoparticles. Figure 15 shows CO IR spectra taken before and after reaction with CH_3OH. The CO probes the available sites at the surface (which are indicated in the figure), and it is clear that the deposited carbon blocks the edge and Pd(100) sites. Similar results indicative of the influence of step edges on dissociation have been found for NO [184]. Indications are found that, in this case, the dissociation products enhance the chemical activity of steps.

A number of studies have also reported on the morphology and structure of Ag [147, 185–187], Au [188–191] and alloy particles on alumina. It is interesting to note that Au, at room temperature, shows a higher degree of dispersion in comparison with Ag. The electronic structure of the coinage metal clusters has been investigated using photon-scanning tunneling microscopy [147], and the dependence of the plasmon on metal, size and alloying has been determined.

It should be noted in passing that the IR spectra of CO as local probes on Pd/alumina model systems may be compared with equivalent data for deposited Pd particles created through wet impregnation from precursor salts on real powder catalysts [192]. When chlorides or nitrates are being used, Lear et al. [192] have shown that there are differences observed that likely stem from precursor residues. The IR spectra of Pd/alumina model systems compare well with real powder catalyst when Pd deposits have been created through the decomposition of $Pd(N_3)_2$ and the metal particles do not contain precursor residues. Dellwig et al. [171] have been able to report vibrational data of CO as a probe molecule on Pd nanoparticles deposited on alumina films as a function of pressure probing from UHV (10^{-10} torr) to 6×10^4 Pa at room temperature. While differences do exist between CO spectra taken at different pressures, and also with respect to equivalent data taken on Pd(111) (which is the orientation of the most abundant facet of the studied Pd nanoparticles), there is no indication for so-called "high-pressure species" in this case [181]. The spectra are also fully reversible as a function of pressure.

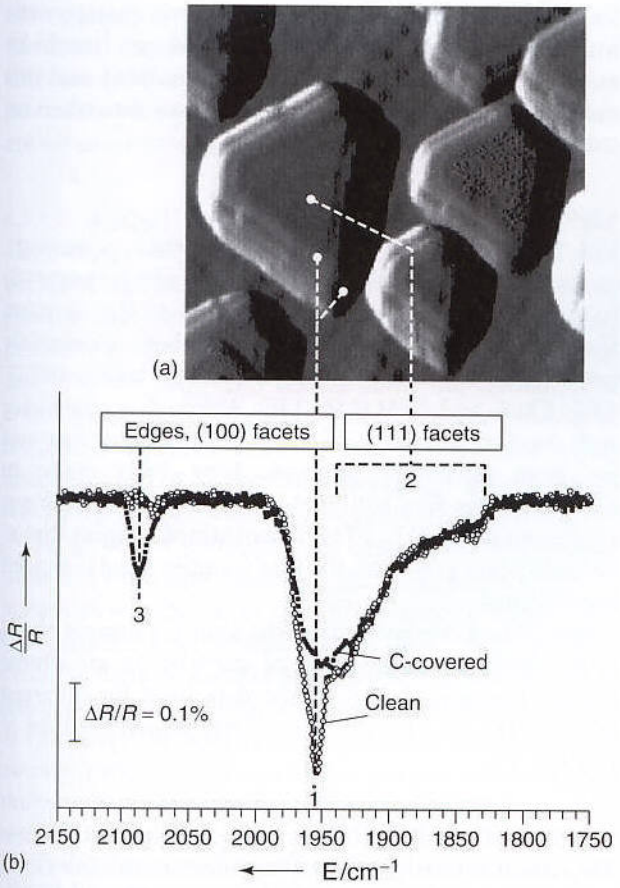

Fig. 15 (a) STM image of the Pd particles grown at 300 K on Al_2O_3/NiAl(110) (20 nm × 20 nm) (from Ref. [343]). (b) RAIR spectra for CO adsorbed on Pd/Al_2O_3/NiAl(110) (sample temperature 100 K, after CO exposure at 300 K); R = reflectivity: open symbols, immediately after preparation; solid symbols, after prolonged exposure to methanol at 440 K [180].

Ethene hydrogenation has been used as a sample reaction to show that the reactivity on nanoparticles is very different to that on single crystals [18, 174, 192–195]. While ethene is not hydrogenated on Pd(111) under UHV conditions, this reaction readily occurs on mainly (111)-terminated Pd/alumina nanoparticles. The reason is simply the influence of subsurface hydrogen at reaction temperatures controlling the nature and amount of the surface hydrogen. Whilst on a bulk single crystal subsurface hydrogen can "escape" into the bulk, in the nanoparticle hydrogen is confined to regions near the surface at all times. This example clearly shows that care must be taken when assuming that single crystal surface studies are always good models to understand processes on particles. In contrast, we are in a position to study how the reactive properties of single crystals evolve, from studies of reactions as a function of particle size. Silvestre-Albero et al. [177, 196, 197] have recently studied butadiene hydrogenation on Pd/alumina model systems as a function of particle size. The measured kinetics show pronounced, characteristic differences between smaller (<5 nm) and larger particles. While the latter particles show a clear correspondence to Pd(111) single crystal surfaces, the former exhibit very different kinetics, providing direct proof that extrapolation from single crystal data to data on facetted particles is not only possible but also provides a limit in size.

The thin alumina films may be chemically modified by hydroxylation [198, 199]. The influence of chemical modification on nucleation, growth and thermal stability of metal deposits is substantial. Both, Rh and Pd have been investigated; in the case of the former, the metal appears to be oxidized and hydrogenation from the OH groups may be desorbed from the metal particle. As the amount of hydroxyls increases, the dispersion of the metal is increased. At the same time, the temperature at which particle sintering becomes appreciable is raised by 100 K [200].

Although thin-film oxide supports are generally well-suited to act as model supports for heterogeneous model catalysts, it has recently been predicted by Pacchioni et al. [201] that there are particular combinations of metals on top of thin oxide films where there is a strong interaction between the deposited metal and the metal crystal supporting the oxide film. This prediction is quite in line with a very early suggestion by Mott [202], which hinted that electrons tunneling between the metal to be oxidized [202] and the growing interface of an oxide film may be rate-limiting. Kulawik et al. [203] recently showed that Au atoms evaporated onto the thin alumina film on NiAl(110) nucleates on Al sites due to this interaction with the substrate, as opposed to oxygen sites which would be the preferred site for Au adsorption on bulk alumina. Pd atoms positions on the film, on the other hand, seem not to be influenced by the underlying metal support, as was also predicted theoretically. Furthermore, in the case of Au on alumina caused by interaction with the underlying metal, the system grows a linear arrangement of Au atoms (see Fig. 16), although without strong direct Au–Au interaction. The formation of the chains is also mediated by the substrate. The results of this study show that care must be taken in choosing appropriate model systems.

In addition to attempts to model dispersed supported metal catalysts, there is increasing activity to model supported oxide catalysts – that is, systems where, for example, a reactive transition metal oxide is supported on a simple metal oxide support. One of the most extensively studied systems appears to be VO_x/alumina/NiAl(110) [17, 204–209].

References see page 1333

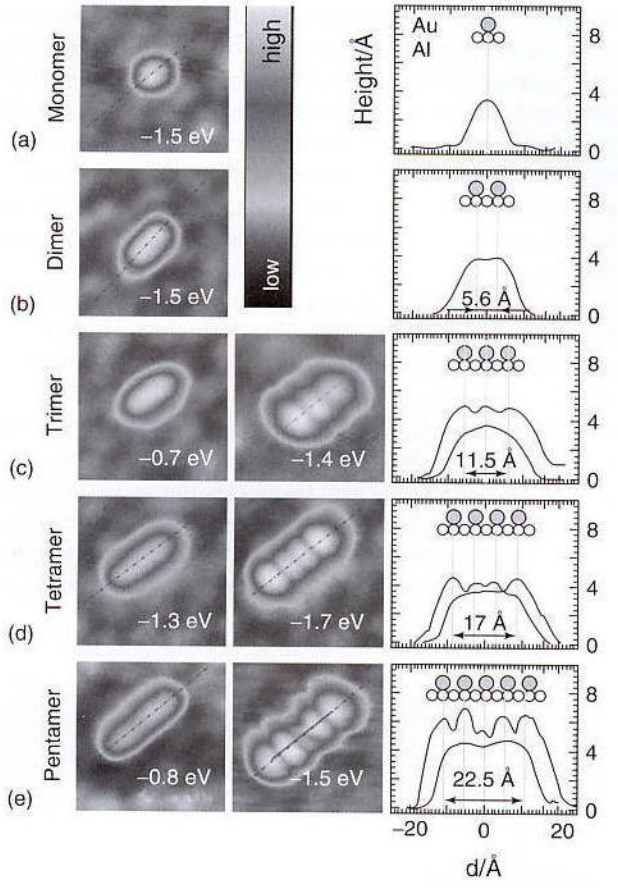

Fig. 16 STM images (43 × 43 Å^2) and according height profiles of a Au monomer (a) and self-assembled Au chains containing two to five atoms (b)–(e) on an alumina film on NiAl(110). The STM images are recorded at negative sample bias V_s, whereby V_s is chosen either well above (left side) or close to (middle) the highest occupied state of the Au chain, as determined by STS [203].

Magg et al. [204–207] have studied the morphology and spectroscopy of vanadium oxide deposits on the thin alumina films prepared by depositing vanadium in a reactive oxygen atmosphere. The transition metal oxide forms clusters which eventually cover the entire alumina surface, but not a continuously wetting film. From a combination of experimental results, together with DFT calculations, it was concluded that the nanoparticles are close to V_2O_3 stoichiometry with average oxidation state V^{3+}, but exposing vanadyl groups at the surface, similar to a $V_2O_3(0001)$ surface, when treated in oxygen. This is unexpected for V_2O_3, as the material does not contain vanadyl groups within the bulk structure. Indeed, it is a pure surface effect. Until the results on $V_2O_3(0001)$ surfaces were published it was assumed that the presence of vanadyl groups is characteristic for V_2O_5, which does contain such groups within the bulk structure. The vanadyl groups were identified via their IR spectrum. On the basis of DFT calculations, a band characteristic for the VO_x/alumina system around 950 cm^{-1} could be assigned to V–O–Al interface vibrations [206], and this made necessary a reassignment of Raman data taken on corresponding powder catalysts.

4.5.4.2 Alumina/$Ni_3Al(111)$

Via the oxidation of a $Ni_3Al(111)$ surface, a smooth, continuous alumina film may be grown which appears to have a similar thickness as compared to the alumina film on NiAl(110). This system has been extensively investigated by Wandelt and coworkers using LEED, AES, EELS, and STM [134–136]. Although a conclusive and detailed structure of the alumina layer has not yet been published, attempts have been made to hydroxylate the film both under UHV as well as ambient conditions [210–213]. STM data obtained suggest that at elevated water pressures the film roughens and is indeed hydroxylated.

One remarkable property of the alumina film on Ni_3Al is its ability to nucleate metal particles in an almost regular hexagonal array. While data exist for different metals [214], the effect is particularly pronounced for V (see Fig. 17).

4.5.4.3 $Al_2O_3(111)$/Ta(110)

The heteroepitaxial growth of thin aluminum oxide films on Ta(110) has been studied [215] using ISS and LEED. The initial film growth was found to be largely two-dimensional, with LEED results indicating the formation of a long-range ordered epitaxial Al_2O_3 film with a slightly distorted ($\beta = 117.9°$) hexagonal lattice. A detailed structural analysis showed that the observed hexagonal pattern can be interpreted as being due to an ordered,

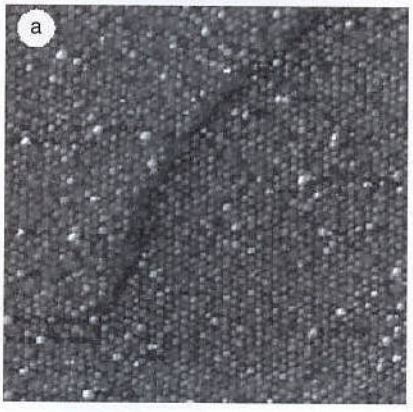

Fig. 17 STM image of V clusters on $Al_2O_3/Ni_3Al(111)$ grown at a substrate temperature of $T_{sub} = 550$ K. The image was taken at a bias voltage of $U_b = 0.7$ V. The tunneling current was $I_t = 100$ pA in both cases. The image size is 125 × 125 nm [214].

close-packed oxygen anion layer associated with either the (0001) face of α-Al_2O_3 or the (111) face of γ-Al_2O_3. Chemically, the Al_2O_3(111)/Ta(110) film is very inert towards a variety of gas molecules, indicating that there are no unsaturated surface bonds.

4.5.4.4 Al_2O_3(111)/Mo(110) and Cu/Al_2O_3(111)/Mo(110)

Thin Al_2O_3 films of various thicknesses have been prepared at room temperature on a Mo(110) surface [216]. Film growth, carried out in an oxygen background pressure of 10^{-4} Pa, was studied using AES, LEED, and HREELS. The AES results show the formation of a stoichiometric Al_2O_3 film, without any indication of metallic aluminum. LEED studies of very thin Al_2O_3 films ($d_{Al_2O_3} \leq 8$ Å) showed a hexagonal pattern which was interpreted as described above for Al_2O_3/Ta(110).

The growth of particulate Cu deposits on these Al_2O_3 films has been investigated in the 80 to 800 K substrate temperature range [216]. The films used to support the Cu particles were typically 20 Å thick, and exhibited excellent thermal stability and chemical inertness toward adsorption. Although particulate metal deposits prepared at relatively low substrate temperatures exhibit smaller average particle sizes and higher particle densities than those prepared at higher temperatures [217–219], the low-temperature preparations are unstable and undergo a major change in morphology and size upon annealing or chemisorption. It was shown that, in order to prepare thermally and chemically stable particles of catalytic interest, it is imperative to carry out the metal deposition at elevated substrate temperatures [216].

TPD spectra of Cu deposited onto an Al_2O_3 film at various substrate temperatures (T_s) show a shift of the peak maxima to higher temperatures and a narrowing of the TPD peak as T_s is increased. It was suggested that the broad TPD peaks observed at low substrate temperatures contain more components and thus reflect a broader size distribution of the Cu particles. Auger measurements showed that Cu particles prepared at $T_s = 600$ K were thermally stable up to an annealing temperature of 850 K, whereas a decrease in Cu Auger intensity was observed upon annealing for those Cu particles prepared at $T_s = 80$ K. A family of TPD spectra of Cu deposited at $T_s = 600$ K is plotted in Fig. 18 as a function of the Cu coverage in equivalent monolayers, θ_{Cu}. The leading edge of the TPD peak shifts continuously toward higher temperatures as θ_{Cu} is increased. At the same time, the TPD peak width remains approximately unchanged as θ_{Cu} is varied over many Cu multilayers. The inset in Fig. 18 shows that the heat of sublimation of Cu particles decreases rapidly from its bulk value of 80 ± 3 kcal mol^{-1} at $\theta_{Cu} \approx 1.2$ to 49 kcal mol^{-1} at $\theta_{Cu} \approx 0.2$. This has been attributed to a decrease in the number of neighboring Cu atoms as the Cu particles become smaller. The average size of the Cu particles estimated from the Auger measurements compares favorably with direct measurements made by TEM.

References see page 1333

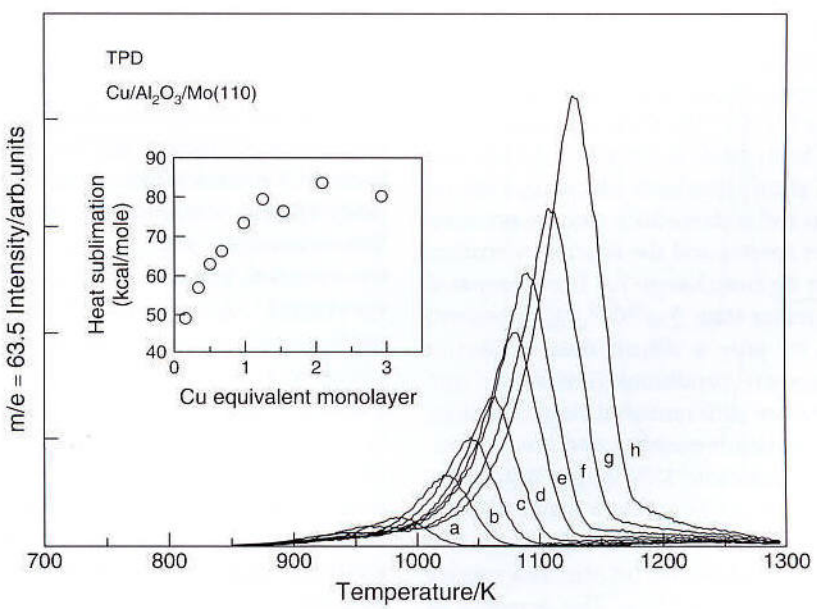

Fig. 18 A family of TPD spectra of Cu deposited on Al_2O_3 films at $T_s = 600$ K as a function of equivalent monolayers, $\theta_{Cu} =$: (a) 0.16; (b) 0.33; (c) 0.50; (d) 0.67; (e) 0.98; (f) 1.25; (g) 1.55; (h) 2.09. The inset shows the heat of sublimation, derived from the leading edge analysis of the spectra, as a function of Cu coverage in equivalent monolayers.

The reaction of nitric oxide and carbon monoxide with particulate Cu deposits supported on Al_2O_3 films has been studied using TPD and HREELS [216]. The surface was exposed to a $^{15}NO/CO$ gas mixture with a ratio of 1:1. At $\theta_{Cu} = 2.7$, corresponding to a cluster size of ≈105 Å, desorption of the parent molecules of ^{15}NO and CO and the gaseous products $^{15}N_2$ and $^{15}N_2O$, due to ^{15}NO decomposition, are observed in TPD. A small CO_2 desorption peak is also observed at temperatures between approximately 150 and 250 K, indicating reaction between CO and ^{15}NO on the supported Cu particles. For small Cu coverages, $\theta_{Cu} = 0.67$, a CO_2 desorption peak was not observed. However, since the CO_2 yield is very small, the effect of particle size on CO_2 production is unclear. Exposure of the clean surface to the $^{15}N_2/CO$ gas mixture gives rise to several adsorbate HREELS features in the 1000 to 2500 cm^{-1} frequency range. Similar to the case for ^{15}NO adsorption, the losses at 1255 and 1465 cm^{-1} were attributed to the $\nu(^{15}NO)$ mode of adsorbed ^{15}NO and $^{15}N_2O$, respectively. The peak loss at 2110 cm^{-1} was due to excitation of the carbon–oxygen stretch $\nu(CO)$ of adsorbed CO.

4.5.5 Silica

Silica is an important catalyst material that is used in many commercial systems as a support [1]. Clearly, a key to the preparation of silica-based model catalysts is the ability to synthesize well-defined thin films of SiO_2.

4.5.5.1 SiO_2/Mo(110)

Thin SiO_2 films may be synthesized on a Mo(110) substrate by evaporating silicon onto the substrate at room temperature in a 5×10^{-4} Pa O_2 background. Such a thin SiO_2 film has been studied with AES, EELS, and IRAS [220, 221]. AES shows that both silicon and silicon dioxide are formed in the intermediate oxygen pressure of 10^{-4} Pa. The Auger spectra and the relative intensities of silicon and oxygen do not change for films prepared at oxygen pressure greater than 5×10^{-4} Pa, consistent with the production of only a silicon dioxide film at the higher oxygen pressure conditions. The silicon and silicon dioxide species are differentiated based on their characteristic Auger transition energies and line shapes. Silicon dioxide has characteristic LVV Auger transitions at 76, 63, and 59 eV, whereas silicon has a major Si(LVV) peak at 91 eV [222, 223]. In addition, an Auger transition energy of 85 eV has been observed for the SiO species on platinum [224] and on silicon [225]. The presence of SiO (silicon monoxide) in the silicon oxide films can be ruled out on the basis of the absence of an Auger transition at ≈85 eV [224, 225]. Such species have only been proposed to exist at the $Si-SiO_2$ interface [226, 227]. Furthermore, the line shapes, the peak energies of the Auger electrons, and the electron energy loss spectra are consistent with those of silicon dioxide. The electron energy loss spectrum for the silicon dioxide films after annealing to 1200 K displays features identical to those of vitreous silica.

The silicon oxide films prepared at room temperature exhibit additional low-energy electron loss features at ≈5 and 7 eV. These features are attributed to a local structure with broken Si–O bonds in tetrahedra of $[SiO_4]$ [228]. Defect-free vitreous silica consists of $[SiO_4]$ tetrahedra connected by an oxygen bridge to form a long-range 3-D network. Thus, the ≈5 and 7 eV EELS features indicate some smaller size $[SiO_4]$ networks.

The intensity of the electron energy loss features at ≈5 and 7 eV is significantly decreased upon heating, and completely disappears after annealing to 1200 K. This behavior demonstrates that the silicon dioxide films undergo structural reorganization to form a long-range 3-D network of $[SiO_4]$.

IRAS further illustrates the structural changes that occur when the silicon dioxide films are annealed. The asymmetric stretch motion of the Si–O bonds appears as a broad asymmetric peak centered at 1178 cm^{-1} in the IRAS spectrum for the film prepared at a substrate temperature of 50 °C. This peak gradually shifts to higher frequency upon heating, and reaches a maximum of 1252 cm^{-1} as the silicon dioxide film is annealed to 1100 °C.

4.5.5.2 SiO_2/Mo(211)

Ordered silica films can be grown on Mo(211), as has been described by Schroeder et al. [229–232]. This film, which exhibits a sharp $c(2 \times 2)$ LEED pattern, was found to have a thickness of 1 ML as estimated from AES intensity attenuation of the Mo(MNN) feature (187 eV) and self-limited growth properties [233, 234]. The orientation and growth of benzene and pyridine were used to characterize the quality of the SiO_2 films via HREELS, AES, and LEED [235]. A single vibrational mode corresponding to the Si–O asymmetric vibration (assigned to a Si–O–Mo) led these authors to propose a structure consisting of isolated $[SiO_4]$ units, as shown in Fig. 19a [233]. Based on more recent studies of the phonon spectrum and electronic calculations [236], the structure has been proposed to be that shown in Fig. 19b. This structure, in contrast to that of Fig. 19a, consists of a 2-D network of SiO_4 tetrahedra where one oxygen is bound to the metal substrate and the other three form a hexagonal honeycomb structure [236]. Resolution of the true structure of monolayer SiO_2/Mo(211) is a subject of ongoing experimental and theoretical studies.

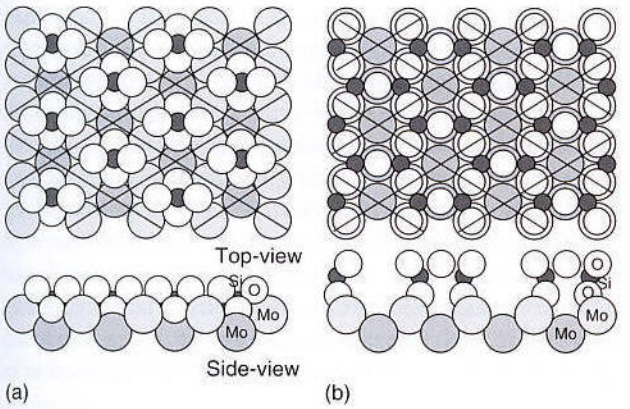

Fig. 19 (a), (b). Top- and side-views of the structural models of isolated $[SiO_4]$ and 2-D network for SiO_2(1 ML)/Mo(112).

4.5.5.3 Cu/SiO_2/Mo(110)

Model silica-supported copper [237–239] catalysts have been prepared by evaporating copper onto a silica thin film grown on MgO(110). The preparation conditions control the corresponding metal particle dispersions or average size [238, 239]. The structure of the model silica-supported copper catalysts has been investigated with IRAS and STM [237, 238]. When deposited at 100 K, copper initially forms a 2-D structure on silica; however, annealing induces the ultrathin copper films (<3 ML) to form small clusters. The unannealed copper films have a significant density of low-coordinated copper sites, whereas the annealed films consist of copper clusters with structures similar to low-index [(111), (110)] and high-index copper planes [(211) or (311)]. The distribution of the facets depends upon the initial copper coverage [237–239]. The desorption energy of copper from the SiO_2 is found to depend markedly on copper coverage (cluster size). A small amount of copper (<0.1 ML) is partially oxidized at the Cu/SiO_2 interface, with the remainder forming 3-D-clusters. Carbon monoxide desorbs in a single peak centered at approximately 210 K from the unannealed copper film, but in several peaks centered between 150 and 220 K from the annealed film. The CO desorption energy depends heavily on the CO coverage, varying from approximately 17 kcal mol^{-1} at the low coverage limit to approximately 1.0 kcal mol^{-1} near CO saturation.

4.5.5.4 Pd/SiO_2/Mo(110)

The adsorption and reaction of CO on silica-supported palladium catalysts over a wide range of temperatures and pressures have demonstrated continuity between catalysis on Pd single crystals [240, 241] and on Pd small particles. The kinetics of CO oxidation at low and high pressures were also shown to be comparable [242, 243]. Pd overlayers of varying thickness on the thin silica films were annealed to 900 K prior to the CO adsorption experiments, producing small metal particles in the range of 30 to 500 Å, with larger particles being formed for the higher Pd coverages.

The IR spectra of adsorbed CO on model silica-supported Pd catalysts are shown in Fig. 20 for Pd coverages of 1.0, 7.0, and 15 ML. The Pd particle size was determined by chemisorption methods [242, 243] and verified using scanning probe techniques. For different Pd coverages, three distinct absorption features corresponding to CO adsorbed onto threefold hollow (1880 cm^{-1}), bridging (1990 cm^{-1}) and atop (2110 cm^{-1}) configurations are observed. At $\theta_{Pd} = 1.0$ ML the dominant absorption feature corresponds to CO adsorbed onto an atop position, while the peaks originating from threefold hollow and bridging CO are broad, suggesting a non-homogeneous distribution of these adsorption sites. Increasing the Pd coverage to 7.0 ML and then to 15 ML results in a sharpening of the absorption features and the dominance of the peak originating from CO adsorbed in the bridging positions. These results demonstrate that

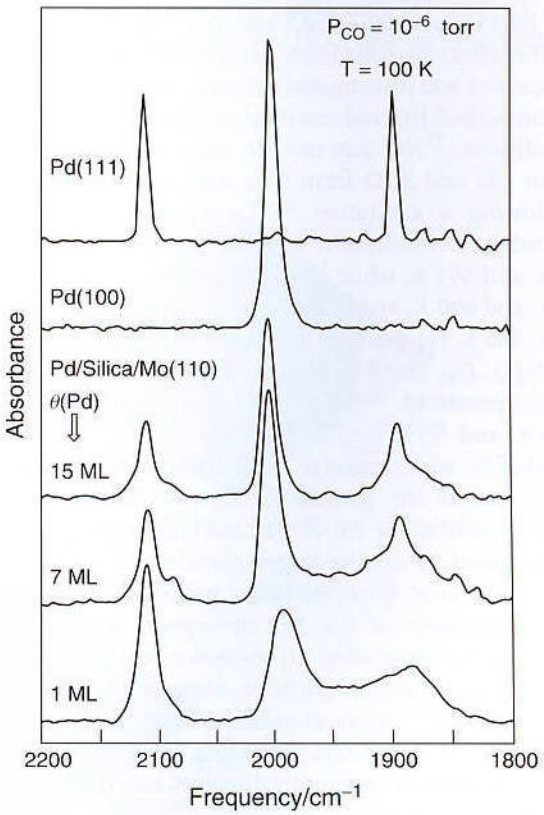

Fig. 20 A comparison of IR reflection-adsorption spectra of CO on Pd(111), Pd(100) and silica-supported palladium surfaces. The spectra were collected at 100 K with a CO pressure of 1×10^{-6} torr.

References see page 1333

the larger particles have well-defined crystal orientations, whereas the smaller particles have a wide distribution of adsorption sites. A comparison of the IR spectra of equilibrated CO overlayers obtained from the $Pd_{15\ ML}/SiO_2$ sample and from the Pd(100) and Pd(111) single crystals reveals striking similarities. The stretching frequencies of adsorbed CO on the model Pd/SiO_2 catalyst (Fig. 20) are identical to the comparable features observed for Pd(100) and Pd(111). The agreement among the IR spectra of the model supported catalysts and the metal single crystals suggests that the metal particles formed on the thin SiO_2 film have facets consisting primarily of (100) and (111) orientation. The formation of metal particles with these Miller indices is thermodynamically favored.

The specific activities of the single crystal and the supported catalysts for CO oxidation are essentially identical [242]. The apparent activation energies for the relatively large particles ($\theta_{Pd} > 2$ ML) are similar ($\approx$27 kcal mol^{-1}), but somewhat lower ($\approx$25 kcal mol^{-1}) for the smaller particles (0.6, 0.3 ML). The apparent activation energies for three Pd single crystals with different orientations are similar [240–243] but distinct: 29.4 ± 0.3 kcal mol^{-1} for Pd(100), 28.1 ± 0.4 kcal mol^{-1} for Pd(111), and 30.7 ± 0.5 kcal mol^{-1} for Pd(110).

The effect of palladium particle size on the catalytic properties was investigated utilizing the decomposition of chemisorbed NO and reactions of NO with CO in flowing conditions. ^{15}NO was used in order to differentiate N_2 from CO and N_2O from CO_2 with mass spectrometry. Following a saturation ^{15}NO exposure on the large particles, ^{15}NO desorbs in three peaks centered at 315, 515, and 595 K, while $^{15}N_2$ is produced in peaks at 545, 595, and 690 K, and $^{15}N_2O$ is evolved in a peak at 545 K. The 545 K N_2 peak is attributed to the fragmentation of N_2O. On small palladium particles ($\approx$50 Å), $^{15}N_2O$ is not produced, ^{15}NO desorbs in two peaks at 310 and 515 K, and N_2 is evolved at 530 and 670 K. The relative yield of N_2 with respect to ^{15}NO desorption (above 400 K) decreases as the particle size grows (from $\approx$50% for 30 Å to $\approx$20% for 250 Å particles), suggesting less NO decomposition on the larger particles. In addition, the formation of N_2O on the larger particles correlates with the appearance of the NO desorption peak at 595 K. There is no detectable O_2 evolution below 1000 K for all sizes of palladium particles. However, O_2 desorption is observed in a peak at $\approx$1250 K, concurrent with the desorption of palladium. Therefore, the oxygen from NO decomposition is apparently dissolved into the bulk of the palladium particles.

The reaction of CO with NO under flowing conditions further demonstrates a particle-size effect. The relative rate of product evolution was monitored with a quadrupole mass spectrometer during reaction with flowing ^{15}NO and CO (1 : 1) at 10^{-4} Pa. The reaction rate increases with increasing catalyst temperature, reaching a maximum at $\approx$580 K, and then declines. On the large palladium particles, the maximum rate of $^{15}N_2O$ evolution occurs at 570 K, some 10 K lower than the maxima for both CO_2 and N_2 production. On the small particles (<50 Å), $^{15}N_2O$ is not produced during the steady-state reaction of a 1 : 1 mixture of ^{15}NO and CO. N_2 is produced by NO dissociation and atomic nitrogen recombination, and CO_2 is produced from the oxidation of CO. The residence time for CO and NO decreases with temperature, whereas the reaction rates increase with temperature leading to an optimum of about 580 K where product formation rate is maximized.

Both the decomposition of NO and the reaction of NO with CO show that the reaction channel for N_2O formation is not available on the small particle (<50 Å). The formation of N_2O requires the simultaneous presence of adsorbed NO and atomic nitrogen at sufficiently high coverages. The temperature-programmed reaction spectra show that the dissociation of NO occurs along the trailing edge of the main NO desorption peak at 515 K. The formation of N_2O correlates with the appearance of the NO desorption peak at 595 K. The higher adsorption energy of the 595 K state increases the NO surface residence time, and thus enhances the probability of N_2O formation by NO combination with atomic nitrogen. On extended single crystal surfaces, N_2O is also formed during the decomposition of NO [244–246]. However, the decomposition of NO and the formation of N_2O correlates with the presence of step/defect (low-coordination) sites on the single crystal surfaces [244–247]. It is likely that there are surface sites with low coordination and varying reactivities on the large particles and extended surfaces. On the perfect (111) and (100) facets, NO desorbs at below 520 K [246, 247], whereas on particles with a variety of low-coordinated sites, NO can decompose to atomic nitrogen and oxygen on some sites, or can be more strongly adsorbed (595 K desorption state) at other sites. The presence of both sites on the large Pd particles, a strong adsorption site for NO, and a second site that promotes decomposition, provides a mechanism for the formation of N_2O. The absence of the N_2O on the small palladium particles can be explained by the lack of the high-temperature NO adsorption state (595 K) which is, in turn, related to the reactivity of the surface sites. The surface of the small particles is more reactive, as indicated by the increased amount of NO dissociation ($\approx$50% for 30 Å and $\approx$20% for 250 Å particles), so that all NO molecules on the low-coordinated sites are likely to be decomposed to atomic oxygen and nitrogen at lower temperatures. The presence of atomic oxygen and nitrogen in the near-surface region will probably further decrease the NO adsorption energy.

4.5.5.5 $Au/SiO_2/Mo(211)$ and $Au/TiO_2/SiO_2/Mo(211)$

Au nanoparticles formed by deposition of Au onto a well-ordered SiO_2 film on Mo(211) are very prone to sintering [248, 249]. This effect can be suppressed by replacing Si atoms in the SiO_2 network by Ti atoms, which may be prepared by evaporating Ti onto the SiO_2 film followed by an anneal [248, 249]. In an STM image acquired subsequently (Fig. 21a), the Ti atoms show up as bright spots. Au evaporated onto this $Ti-SiO_2$ surface form clusters that reside on top of the Ti defect sites (Fig. 21b). Further evaporation of Ti onto the surface of Fig. 21a leads to the formation of needle-like islands of TiO_x on the silica network (see Fig. 21c). Au evaporated onto this surface decorates exclusively as clusters at the termini of the titania islands (as shown in Fig. 21c) and is extremely resistant to thermal sintering. The origin of the unusual stability of the Au clusters is not fully understood, but is thought to relate to the unusual strong interaction between Au and the TiO_x structures arising from the enhanced defect density at their termini.

4.5.6 Titania

Titania is an important reducible oxide which often is used as a catalyst/photocatalyst or as a catalyst support. Thin films of titania with various stoichiometries have been prepared on single crystal surfaces of Mo(110), Mo(211), Pt(111), Ni(110), and W(100). These thin-film preparations, along with their bulk single crystal counterparts, have been extremely valuable in developing an understanding of the role of surface defects in the surface chemical properties of this important oxide material as well as the role of defects in nucleating and stabilizing supported metal clusters.

4.5.6.1 $Ti_xO_y/Mo(100)$, Mo(110), Pt(111), Ni(110), W(100)

Ultrathin (<100 Å) titanium oxide films can be synthesized on the Mo(100) surface [250]. Epitaxial growth with varying film thickness were revealed by ISS, XPS, and AES. LEED showed a $(2\sqrt{2} \times \sqrt{2})R45°$ diffraction pattern, whereas STM images showed that the TiO_2 films were ordered along the [010] and [001] directions of the Mo(100) substrate. XPS data revealed that unannealed titanium oxide films exhibit only a Ti^{4+} valence state, whereas annealed titanium oxide films are partially reduced and exhibit Ti^{3+} and Ti^{2+} states.

Ordered titanium oxide films can also be grown epitaxially on a Mo(110) substrate [251, 252]. Using various synthetic methods, $TiO_2(100)$ or $Ti_2O_3(0001)$

References see page 1333

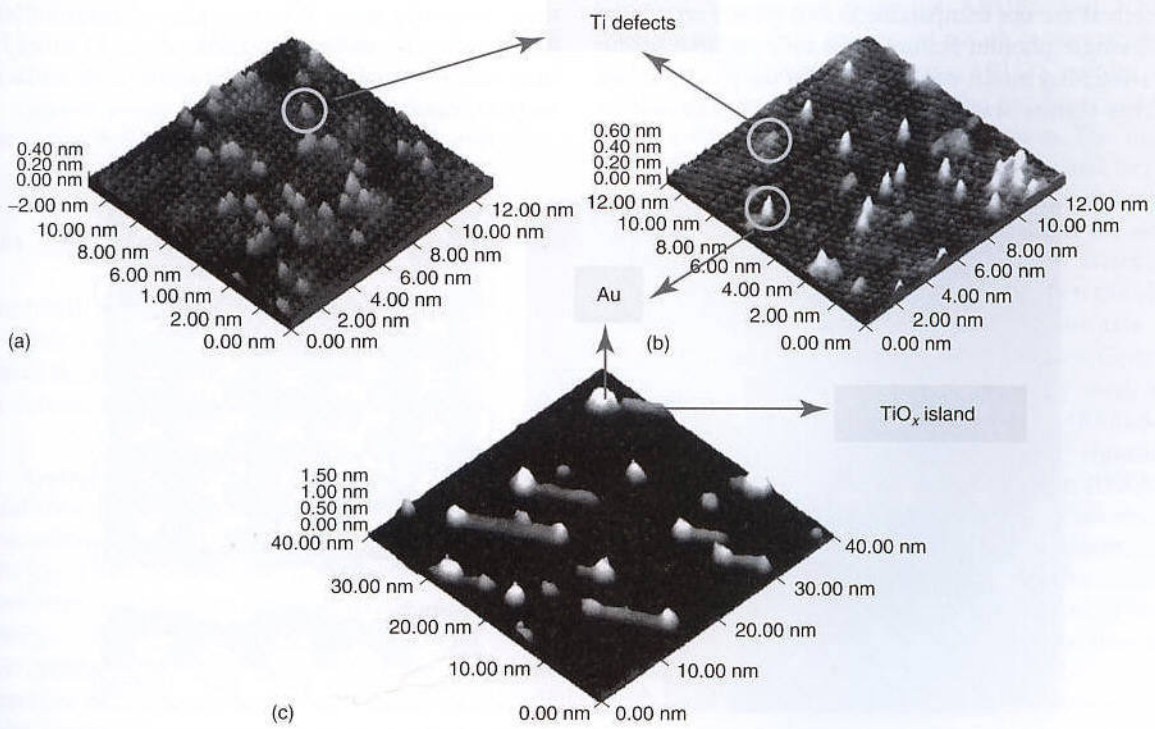

Fig. 21 3-D STM images of (a) TiO_x (8%)$-SiO_2$; (b) Au (0.04 ML)/TiO_x(8%)$-SiO_2$; (c) Au (0.08 ML)/TiO_x (17%)$-SiO_2$, showing that both Ti defects and TiO_x islands play a role as nucleation sites for Au clusters [248].

were synthesized, as evidenced by (1 × 1) rectangular and (1 × 1) hexagonal LEED patterns, respectively, with supporting data from AES and XPS. STM indicated layer-by-layer growth at 900 K, and the presence of flat terraces with three different orientations. The spacings between the neighboring atomic rows for all terraces were similar (0.65 nm), suggesting epitaxial growth of TiO_2(110)-(1 × 1). TiO_2 films have also been grown on Pt(111) [253], Ni(110) [254, 255] and W(100) [256].

4.5.6.2 Au/TiO_x/Mo(211)

A well-ordered monolayer titanium oxide film, Mo(112)-(8 × 2)-TiO_x, can be synthesized on the Mo(112) surface [77, 257]. The TiO_x/Mo(112) film was synthesized by depositing ≈1 ML Ti onto a SiO_2(ML)/Mo(112) following subsequent oxidation/annealing. A final anneal at 1400 K completely removes the SiO_2 film and any residual Si. The TiO_x film so formed exhibits a very sharp (8 × 2) LEED pattern (Fig. 22), and a very smooth and well-ordered surface that exhibits relatively large terraces, as seen by STM images (Fig. 22). The thickness of this TiO_x film is estimated to be one monolayer, based on the attenuation of the AES intensity of the Mo MNN (187 eV) feature. The (8 × 2)-TiO_x film can also be synthesized by the step-wise direct deposition of Ti onto an oxygen-covered Mo(112) surface followed by subsequent oxidation–annealing cycles. However, the quality and reproducibility of the film derived from the direct deposition method are not comparable to that grown on a SiO_2 film. A single phonon feature at 84 meV, related to the Ti–O stretching mode, was observed for the (8 × 2) structure. This feature was assigned to Ti^{3+}–O–Mo and/or Ti^{3+}–O–Ti^{3+} based on HREELS and XPS data [77, 257]. A row spacing of 0.9 nm, corresponding to two rows of the Mo(112) trough along the [−110] direction, is seen by STM (Fig. 22), consistent with the observed (8 × 2) LEED pattern (Fig. 22). A high-resolution STM image shows a double-row feature with a spacing of 0.9 nm. A possible structural model for the Mo(112)-(8 × 2)–TiO_x surface is shown in Fig. 22 in which seven Ti atoms decorate every eight Mo atoms along the Mo(112) trough (the [−1 −11] direction). The Ti atoms are bound to the surface via Ti–O–Mo bonds, and to each other via Ti–O–Ti linkages [77, 257–259].

On the rutile TiO_2(110) surface the two Ti atoms nearest to an oxygen vacancy are reduced to Ti^{3+}, whereas for the (8 × 2)-TiO_x surface there is a full monolayer of reduced Ti^{3+} sites [77, 257]. Accordingly, strong binding between deposited Au and the TiO_x surface is anticipated. Indeed, upon deposition of Au onto this (8 × 2)-TiO_x surface followed by an anneal at 900 K, well-ordered Au monolayer and bilayer structures form with Au completely wetting the surface [77, 259]. The two ordered structures, designated as (1 × 1) Au–TiO_x mono- and (1 × 3) Au–TiO_x bi-layer, respectively, are shown schematically in Fig. 23a and b [77, 259]. Temperature-programmed desorption (TPD) indicates that the Au–TiO_x interaction is much stronger compared to the Au–Au interaction [259]. Kinetic measurements for the catalytic oxidation of CO show that the (1 × 3) Au–TiO_x bilayer is significantly more active (by more than an order of magnitude) than the monolayer (see Fig. 24), and is about 45 times higher than that reported for the most active high-surface-area Au/TiO_2 catalyst [77, 260].

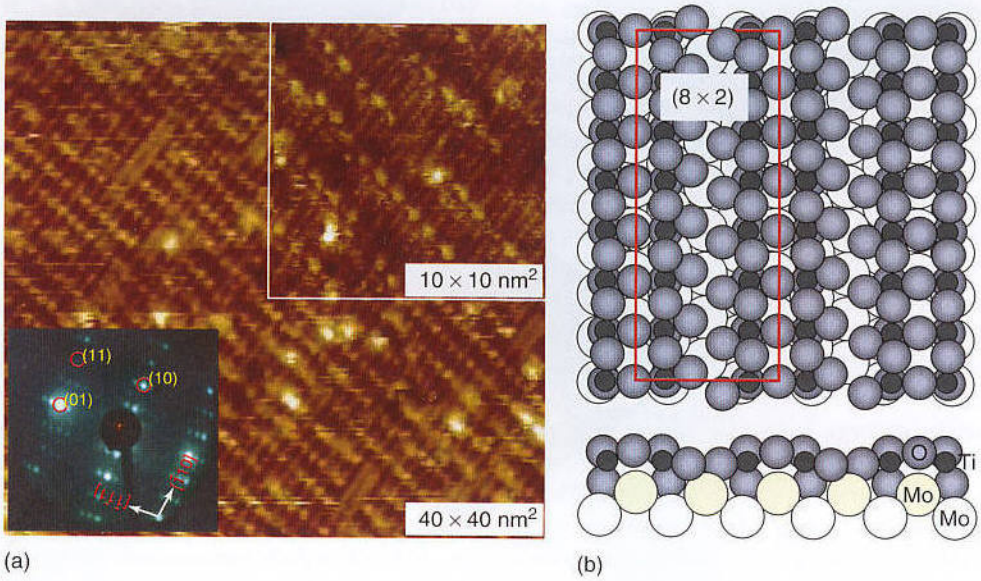

Fig. 22 (a) An atomically resolved STM image and a structural model for Mo(112)-(8 × 2)-TiO_x. The insert shows a (8 × 2) LEED pattern.

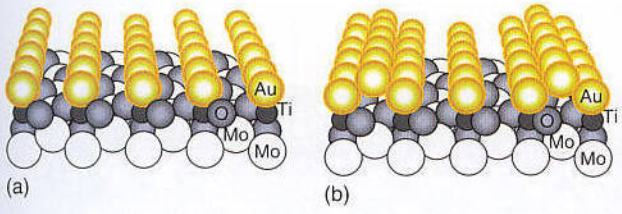

Fig. 23 (a) A structural model of the (1 × 1)-(Au,TiO_x) monolayer; and (b) a structural model of the (1 × 3)-(Au, TiO_x) bilayer [77, 257, 259].

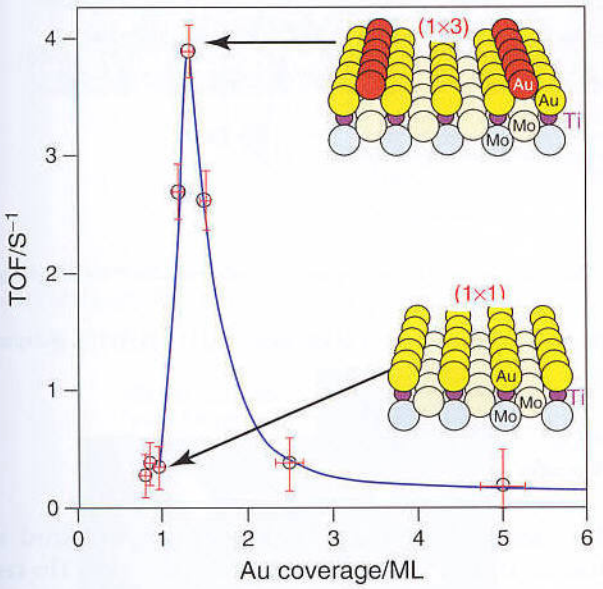

Fig. 24 Catalytic activity for CO oxidation as a function of Au coverage on the Mo(112)-(8 × 2)-TiO_x at room temperature [77].

4.5.7 Chromia

Chromium(III) oxide, Cr_2O_3, is one of the most active oxide catalysts and catalyzes reduction of NO, hydrogenation of alkenes, dehydrogenation of alkanes, alkene polymerization, and methanol synthesis.

4.5.7.1 Cr_2O_3(111)/Cr(110)

Epitaxial Cr_2O_3 films can be grown on the Cr(110) surface by oxidation of the Cr(110) surface at 550 K and 10^{-4} Pa O_2. The Cr_2O_3(111)/Cr(110) surface and its adsorption behavior have been extensively characterized [98, 261–265].

LEED, STEM, and RHEED studies [261, 266–269] show the presence of a rhombohedral, epitaxial Cr_2O_3 oxide film with its (111) surface parallel to the Cr(110) surface of the substrate. The ARUPS, XPS, and NEXAFS results show that both occupied and unoccupied states for this film are very similar to those of the bulk Cr_2O_3 oxide. The band structure of the film, measured by ARUPS, shows a pronounced dispersion along the surface normal, indicating the formation of a 3-D band structure, despite a thickness of only 6 nm. The vibronic structure of this film, as determined by HREELS, compares well with the vibronic structure of the bulk oxide measured by IR. Electron energy loss spectra, combined with adsorption experiments, have shown that the Cr ion in the surface layer has a different oxidation state than in the bulk. The adsorption of O_2, CO, NO, CO_2, NO_2, H_2O on the Cr_2O_3(111)/Cr(110) surface has been studied using LEED, TPD, ARUPS, XPS, NEXAFS, ELS, and HREELS.

Chromium oxide, under reducing conditions, is terminated by half a Cr ion layer depolarizing the (0001) surfaces. If the surface is exposed to oxygen, a molecular oxygen species is formed which then transforms into chromyl groups with Cr=O double bonds [270].

The chromyl bonds have a very characteristic vibrational bond at 1040 cm^{-1}. Chromyl-terminated surfaces show considerably less tendencies for adsorption than the metal-terminated, reduced surface. Reduction can be achieved by heating *in vacuo*.

CO has been found to be only weakly chemisorbed (T_d = 160 K) on the surface, forming an ordered ($\sqrt{3} \times \sqrt{3}$)R30° structure. Upon saturation of the surface with O_2, CO is not adsorbed, indicating that CO adsorbs on Cr-terminated sites. The adsorption geometry for CO was determined from the ARUPS and NEXAFS measurements, and confirmed via *ab initio* calculations [273, 274, 276]. Figure 25 shows ARUPS results, taken with a fixed angle (90°) between the incident light beam and the direction of the electron detection. The incident light angle with respect to the surface normal has been varied from 10° to 80°. The peaks at 11.8 and 14.3 eV have been attributed to the emissions from the 4σ and 5σ valence states of CO. Since the σ valence states of CO emit strongest along the molecular axis when the electric field vector of the exciting light is along this axis, these results indicate that CO lays flat on the surface. Consistent with this adsorption geometry, only a very weak signal of CO vibration has been observed in HREELS. The intensity of the π resonance does not change significantly with increasing angle of the incident light in NEXAFS.

Starting from this structure, photodesorption studies of CO resolving the translational and internal degrees of freedom of the desorbing molecules including the orientation of the rotational axis have been undertaken [271–278]. Depending on rotational excitation, cartwheeling as well as helicoptering molecules are desorbed.

NO also adsorbs molecularly on this surface, but desorbs at 350 K. As determined by ARUPS and NEXAFS,

References see page 1333

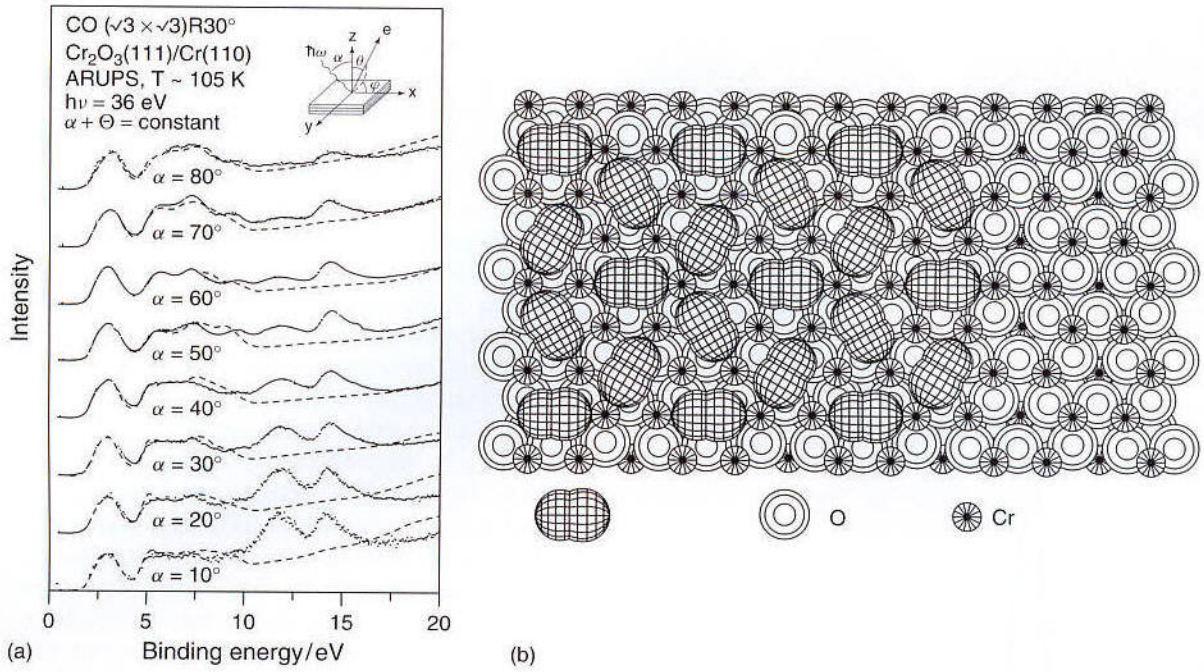

Fig. 25 (a) ARUPS spectra of CO an the Cr_2O_3(111)/Cr(110) surface; (b) the proposed structure of CO an Cr_2O_3(111)/Cr(110). (Adapted from Ref. [262].)

NO is tilted by 30° with respect to the surface normal. The photodesorption of NO has also been studied [279]. By contrast, NO_2 and CO_2 react with the surface even at 100 K. At low NO_2 exposures and low temperatures, NO_2 dissociates to NO and O, while at higher NO_2 doses, N_2O_4 starts to form on the surface. CO_2 reacts with the surface at 100 K, forming carboxylate in addition to physisorbed CO_2. From NEXAFS, ARUPS, and HREELS measurements, it was determined that carbonate is bound to the surface in a bidentate configuration. H_2O either physisorbs or chemisorbs molecularly on the surface, but dissociates to form adsorbed OH in the presence of defect sites or under the influence of photon irradiation.

Adsorption of Na on Cr_2O_3(111)/Cr(110) has been studied by Ventrice et al. [264] using HREELS and ARUPS (Fig. 26), and photodesorption of K from the same surface by Wilde et al. [280]. The presence of 2 ML Na almost completely quenches the optical phonon branch, indicating the metallic nature of the adsorbed Na. Adsorption of CO_2 or H_2O on this Na-precovered surface completely restores the optical phonon peak. Since ARUPS does not show any recovery of emission from Cr_2O_3, these results clearly indicate a metal-to-non-metal transition. This is supported by the ARPES results, which show a suppression of emission from the Fermi level, the disappearance of the LVV Auger transition, and a shifting to higher binding energy of the Na(2p) emission upon compound formation during coadsorption.

4.5.8 Vanadia

In recent years a number of groups have started to investigate thin vanadium oxide films [281–287]. The vast majority of studies have been carried out for V_2O_3(0001) surfaces. Here, we will concentrate on this particular surface and only mention in passing that some studies have been conducted on a variety of stoichiometries that are found on Rh(111) [285] and Pd(111) [282–284] supports, as well as thin V_2O_5 films [288].

4.5.8.1 Vanadium Sesquioxide

V_2O_3(0001) surfaces have been prepared by reactive metal deposition on a number of metal substrates including Au(111) [281, 286, 287], W(110) [286], Rh(111) [285], and Pd(111) [282–284]. Figure 27 shows an STM image of a V_2O_3(0001) surface [208]. V_2O_3(0001) is isostructural to Cr_2O_3(0001). We therefore expect a metal-terminated surface with half of the ion positions filled. However, vibrational spectroscopy has indicated that each of the metal ions is doubly bound to oxygen atoms, forming VO_4 tetrahedra with the vanadyl bond perpendicular to the surface [286, 287], similar to Cr_2O_3(0001).

The regular protrusions represent the vanadyl groups, that is, the oxygen at the apex of the VO_4 tetrahedra. The separation of the protrusions is in accordance with this assignment. Also, DFT calculations support

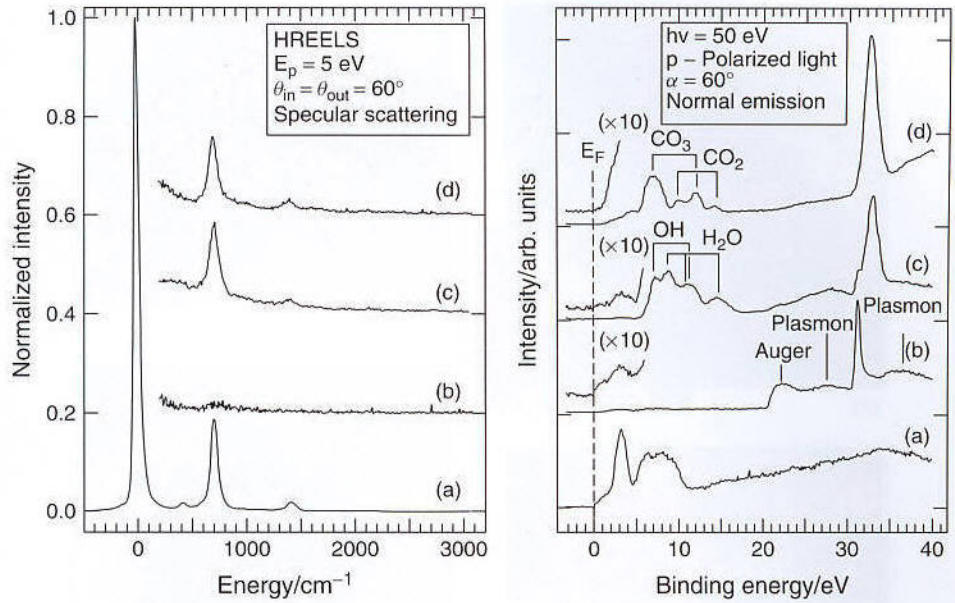

Fig. 26 High-resolution electron energy loss (EEL) (left) and ARUPS (right) spectra of: (a) a clean $Cr_2O_3(111)/Cr(110)$ surface; (b) with 2.2 ML of Na adsorbed onto the surface; (c) 4 L of water coadsorbed; (d) 20 L of CO_2 coadsorbed with 2.2 ML of Na.

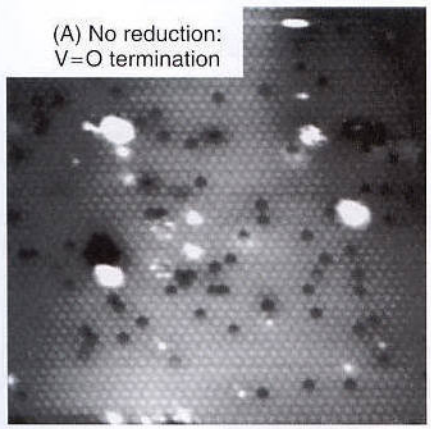

Fig. 27 STM images of vanadia nanoparticles deposited on a model silica surface ($SiO_2/Mo(112)$). Image: 100 × 100 nm, $U = 3$ V, $I = 0.2$ nA [208].

that a vanadyl-terminated surface is the most stable one under oxygen-rich conditions. The surface may be reduced by electron bombardment (in contrast to $Cr_2O_3(0001)$, where the Cr=O bonds could be removed thermally), which leads to a removal of the vanadyl oxygen without changing the periodicity of the surface layer as indicated (see Fig. 26). It is this reduced surface that adsorbs CO [208] and is able to oxidize CH_3OH to formaldehyde [289], while the completely vanadyl-terminated surface is unreactive. Electronically, the vanadyl-terminated surface carries a top layer of V^{5+} ions, as recently clearly demonstrated by synchrotron-based XPS measurements, while the deeper layers contain V^{3+} ions [286]. The formation of the vanadyl groups by adsorption from molecular oxygen in the gas phase can be followed by IR spectroscopy. DFT calculations show that the molecular oxygen species represents a peroxospecies O_2^{2-} which is bound edge-on to the surface vanadium ions. This species then transforms into the vanadyl groups.

4.5.9 Iron oxides

Iron oxide is a technologically important transition metal oxide used in a number of catalytic processes, including styrene production, methanol oxidation to formaldehyde, and the water-gas shift reaction. The synthesis of thin-film models with well-defined stoichiometries is important in developing an understanding of the relationship between the structure of such surfaces and their chemical function.

4.5.9.1 FeO/Pt(111), $Fe_2O_3(0001)$/Pt(111), $Fe_3O_4(001)$/Pt(111)

Iron oxide films of high quality and varying stoichiometry can be grown on Pt(111). The growth and properties of such films have been reviewed recently by Ranke and Weiss [290]. The STM images of three different oxides are shown, together with their unit cell

References see page 1333

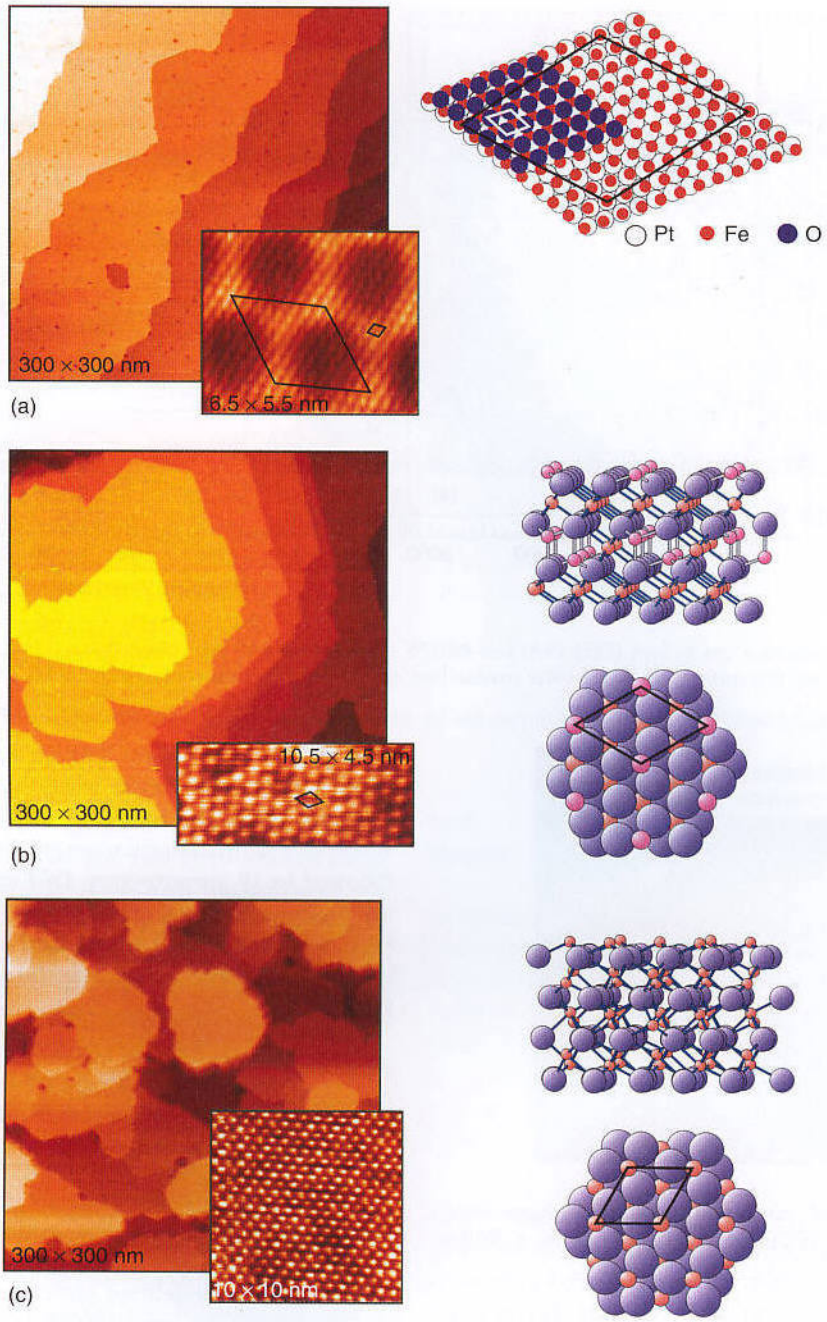

Fig. 28 STM data (morphology and atomically resolved images) and schematic structure representations for: (a) FeO(111)/Pt(111); (b) $Fe_2O(001)/Pt(111)$; and (c) $Fe_2O_4(111)/Pt(111)$.

and parameters determined by structural techniques, in Fig. 28. The FeO(111) represents a two-layered clean film with oxygen termination [291–296]. The $Fe_2O_3(0001)$ surface is isostructural to chromia and alumina. Experiments have indicated that two different surface terminations exist on $Fe_2O_3(0001)$ [297–301]. Thornton et al. have found even a bi-phase termination with different stoichiometries coexisting on bulk single crystal surfaces [302]. The terminations were corroborated via DFT calculations which indicated that a $Fe_2O_3(0001)$ film exhibits the typical half-layer iron termination, and coexisting with it an oxygen termination with [297]. Recent experiments have indicated that there is a rather stable ferryl Fe=O termination similar to $Cr_2O_3(0001)$ and $V_2O_3(0001)$. For $Fe_3O_4(111)$, several models have been proposed [303–305].

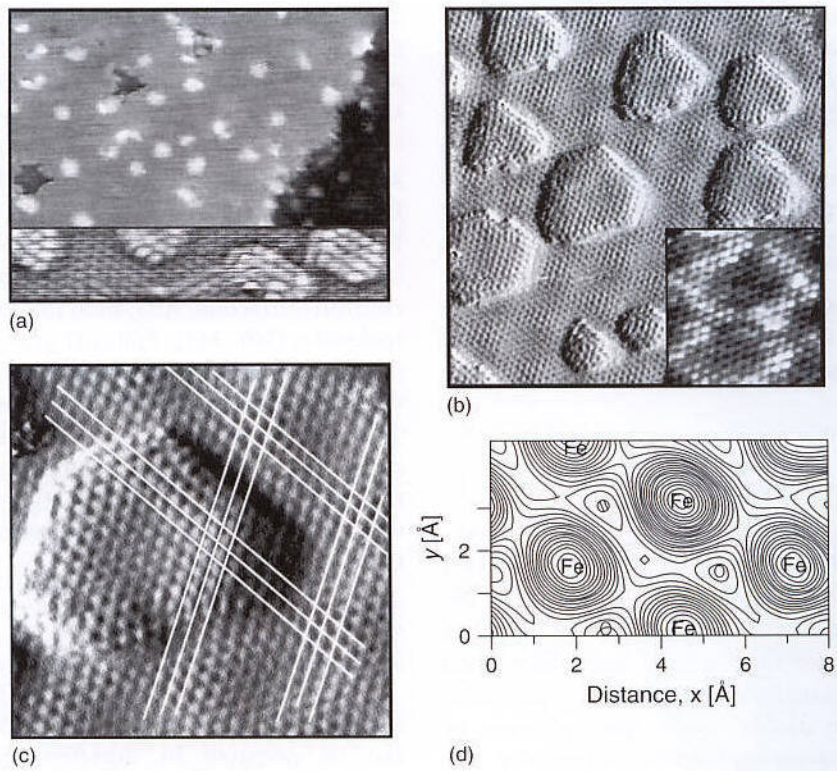

Fig. 29 (a) A STM image of 0.05 ML Pd deposited on a FeO film at 130 K shows random nucleation of the particles (size 39 × 22 nm^2, V_{tip} = 200 mV, I = 2 nA). The atomic structure of the Pd deposits exhibiting the (111) surface is resolved in the inset (−9 mV; 1.8 nA). (b) STM image, presented in differentiated contrast, of the extended Pd(111) islands formed by deposition of 0.5 ML of Pd at 130 K and subsequent annealing to 600 K (20 × 20 nm^2, 2 mV, 4.5 nA). The surface of the large Pd(111) islands exhibits a long-range modulation, as shown in the inset (4.8 × 4.8 nm^2, −20 mV, 5 nA). (c) Registry analysis of the Pd(111)=FeO(111) interface shows that Pd atoms occupy hollow sites over the lattice of protrusions imaged on FeO (6 × 6 nm^2, 2 mV, I = 5 nA). (d) Contour plot of the lowest unoccupied DOS near Fermi level for the FeO film showing the maxima over the Fe ions [306].

4.5.9.2 Pd, Au on Iron Oxides

Pd and Au form 2-D or 3-D islands on FeO(111)/Pt(111) [306–309], depending on the preparation conditions. At low temperature, Au self-organizes into a hexagonal pattern [310]. If Pd deposits are heated above 500 K, the Pd migrates to the FeO/Pt interface, forming 2-D islands (as shown in Fig. 29). Au has a tendency to stay on top of the FeO(111) surface forming 2-D islands at low temperature and 3-D aggregates at elevated temperatures. CO desorption and IR experiments have shown that the smaller Au aggregates bind CO more strongly than larger aggregates, the adsorption behavior of which quickly converges to the properties observed for a bulk gold surface.

Au deposits have also been studied on Fe_2O_3(0001) and Fe_3O_4(111) surfaces [74, 191]. The results correspond to a large extent to those at FeO(111) surfaces.

Recently, Pd/Fe_3O_4(111) have been intensively studied with respect to their structure and reactivity; that is, to CO oxidation after preoxidation in an oxygen atmosphere [311–315]. It transpires that oxygen chemisorbs on the Pd particles, the morphology of which is similar to that found for Pd/alumina surfaces, at room temperature, while at higher temperatures the oxygen migrates into the particles and forms a Pd oxide primarily at the interface between the particular and the iron oxide support [311]. The formation of the interfacial oxide leads to a reshaping of the Pd nanoparticles upon reduction with CO via CO oxidation. The Pd oxide formation also has dramatic consequences for the kinetics of CO oxidation, which is strongly particle size-dependent [313]. In general, the formation of the Pd oxide reduces the CO oxidation activity.

4.5.10 Niobia

Thin niobia films with long-range order have been prepared by Niehus et al. on the surface of a Cu_3Au(100)

References see page 1333

alloy [316, 317] and on Pt(111) [318, 319]. Films of different thickness seem to expose different surfaces, as characterized by combining STM, EELS, FTIR, TDS, and XPS. The stoichiometry of the oxide is near Nb_2O_5, but the surface termination appears to depend on the thickness of the layer. There is a surface which contains Nb=O (niobyl) groups, except for a bulk-terminated thicker film and the surface of a thinner film, which does not exhibit such groups.

Pd has been deposited on niobia films, and there appears to be a very strong interaction involving oxidation of the deposited transition metal by the niobia film [320].

4.5.11 Molybdenum Oxide

Molybdenum oxide films have been grown on Mo(110) surfaces by Friend et al. [321–326], although a detailed structural characterization with atomic detail is still lacking. A number of structural units have been identified by vibrational spectroscopy, in particular molybdenum oxygen double bonds. The influence of such structural units on hydrocarbon chemistry has been studied in some detail. Nitrous oxide adsorption has also been investigated [327–330]. More recently, MoO_3 films have been grown on Au(111), while LEED, STM, photoemission and X-ray absorption studies are becoming available on these compounds [331–333].

4.5.12 Ceria

CeO_2(111) films have been studied on several substrates, including Pt(111) [334, 335], Cu(111) [336], Ni(111) [337], Ru(0000) [337], Re(0001) [338], and Rh(111) [339]. The oxide films have been characterized using XPS, LEED, EELS, and STM. Molecular adsorption has been studied involving CO and NO molecules, and a limited number of experiments have also been reported on Rh deposition on those films [148].

4.5.13 Binary Oxides

Thin oxide films supported on dissimilar oxides are often found to provide enhanced catalytic properties, with V_2O_5 supported on anatase TiO_2 being a well-known example. Although the nature of the interaction of the underlying oxide support on an oxide overlayer is still poorly understood, thin-film oxide preparations of one oxide on another can provide tractable models for delving into this important, yet complex, problem. To date, very few studies have addressed the important topic of layered-mixed oxide surfaces (see also the review by Chambers [4]).

4.5.13.1 NiO/MgO, NiO/CaO, MgO/NiO, CaO/NiO/Mo(100)

Layered, binary thin-film oxides of NiO, MgO and CaO have been prepared and characterized using low-energy electron diffraction, AES, ELS, ISS, and TPD using probe molecules [340, 341]. Epitaxial growth was observed for the NiO–MgO and CaO–NiO systems; however, superior wetting was found for NiO–MgO relative to CaO–NiO. The thermal stabilities of the supported monolayer oxide vary significantly for the four systems studied; that is, NiO/MgO, NiO/CaO, MgO/NiO and CaO/NiO, with NiO/CaO having the lowest thermal stability and CaO/NiO, the highest.

4.5.14 Conclusions

Recent studies have shown that model oxide surfaces can be prepared in thin-film form, a preparation strategy that readily enables their exploration with a wide array of charged-particle surface techniques. Such investigations offer unprecedented opportunities to address the molecular details of the chemistry at oxide surfaces. Furthermore, the addition of metals to the oxides as supports provides a convenient method to model important aspects of supported-metal catalysts such as support–particle interactions and quantum-size effects of supported-metal particles. Using such model catalysts, an array of surface-science techniques can be implemented to study catalysis by metals in systems with well-defined particle sizes and morphology.

In combination with technical advances in operando techniques, such as sum frequency vibrational spectroscopy, polarization modulation IRAS, and various synchrotron-based X-ray spectral/diffraction probes, this approach to studying model catalysts allows the so-called "pressure and material gaps" to be bridged simultaneously. These investigations offer a range of new opportunities to directly connect studies of single crystals and ordered thin films under UHV environments with analogous investigations of catalytic processes of "real world" catalysts under realistic operating conditions.

Acknowledgments

D. W. G gratefully acknowledges support by the Department of Energy, Office of Basic Energy Sciences,

Division of Chemical Sciences, and the Robert A. Welch Foundation. H. J. F. acknowledges support by the Deutsche Forschungsgemeinschaft through the Sonderforschungsbereich 546 (Structure, Dynamics and Reactivity of Aggregates of Transition Metal Oxides) as well as by the Fonds der Chemischen Industrie, and the European Union through the GSOMEN Project (Growth and Supra-Organization of Transition and Noble Metal Nanoclusters).

References

1. G. Ertl, H. Knözinger, J. Weitkamp (Eds.), *Handbook of Heterogeneous Catalysis*, Wiley-VCH Verlagsgesellschaft mbH, Weinheim, 1997.
2. V. E. Henrich, P. A. Cox, *The Surface Science of Metal Oxides*, Cambridge University Press, Cambridge, 1994.
3. H.-J. Freund, H. Kuhlenbeck, V. Staemmler, *Rep. Progr. Phys.* **1996**, *59*, 283.
4. S. A. Chambers, *Surf. Sci. Rep.* **2000**, *39*, 105.
5. H.-J. Freund, H. Kuhlenbeck, M. Neumann, in *Adsorption on Ordered Surfaces of Ionic Solids and Thin Films*, Vol. 33, E. Umbach, H.-J. Freund (Eds.), Springer-Verlag Berlin Heidelberg, Berlin, 1993, pp. 136.
6. R. Franchy, *Surf. Sci. Rep.* **2000**, *38*, 195.
7. H.-J. Freund, *Ber. Bunsenges. Phys. Chem.* **1995**, *99*, 1261.
8. H.-J. Freund, *Angew. Chem. Int. Ed. Engl.* **1997**, *36*, 452.
9. M. Bäumer, J. Libuda, H.-J. Freund, in *Chemisorption and Reactivity on Supported Clusters and Thin Films*, Vol. 331, R. M. Lambert, G. Pacchioni (Eds.), Kluwer, Dordrecht, 1997, p. 61.
10. H. Kuhlenbeck, H.-J. Freund, in *Growth and Properties of Ultrathin Epitaxial Layers, The Chemical Physics of Solid Surfaces*, Vol. 8, D. A. King, D. P. Woodruff (Eds.), Elsevier, New York, 1997, p. 340.
11. G. Ertl, H.-J. Freund, *Physics Today* **1999**, *52*, 32.
12. M. Bäumer, H.-J. Freund, *Progr. Surf. Sci.* **1999**, *61*, 127.
13. H.-J. Freund, M. Bäumer, H. Kuhlenbeck, *Adv. Catal.* **2000**, *45*, 333.
14. H.-J. Freund, N. Ernst, T. Risse, H. Hamann, G. Rupprechter, *Phys. Stat. Sol. (a)* **2001**, *187*, 257.
15. H.-J. Freund, *Surf. Sci.* **2002**, *500*, 271.
16. H.-J. Freund, J. Libuda, M. Bäumer, T. Risse, A. F. Carlsson, *Chem. Rec.* **2003**, *3*, 181.
17. H. J. Freund, *Catal. Today* **2006**, *117*, 6.
18. H.-J. Freund, *Catal. Today* **2005**, *100*, 3.
19. J. Libuda, H.-J. Freund, *Surf. Sci. Rep.* **2005**, *57*, 157.
20. D. W. Goodman, *Surf. Rev. Lett.* **1995**, *2*, 9.
21. M. C. Wu, J. S. Corneille, C. A. Estrada, J.-W. He, D. W. Goodman, *Chem. Phys. Lett.* **1991**, *182*, 472.
22. J.-W. He, C. A. Estrada, J. S. Corneille, M.-C. Wu, D. W. Goodman, *Surf. Sci.* **1992**, *261*, 164.
23. M. C. Wu, C. A. Estrada, D. W. Goodman, *Phys. Rev. Lett.* **1991**, *67*, 2910.
24. M. C. Wu, C. A. Estrada, J. S. Corneille, D. W. Goodman, *J. Chem. Phys.* **1992**, *96*, 3892.
25. J.-W. He, J. S. Corneille, C. A. Estrada, M. C. Wu, D. W. Goodman, *J. Vac. Sci. Technol. A – Vacuum Surfaces & Films* **1992**, *10*, 2248.
26. M. C. Wu, D. W. Goodman, *Catal. Lett.* **1992**, *15*, 1.
27. M. C. Wu, C. M. Truong, K. Coulter, D. W. Goodman, *J. Am. Chem. Soc.* **1992**, *114*, 7565.
28. M. C. Wu, C. M. Truong, D. W. Goodman, *Phys. Rev. B* **1992**, *46*, 12688.
29. M. C. Wu, C. M. Truong, K. Coulter, D. W. Goodman, *J. Vac. Sci. Technol. A – Vacuum Surfaces & Films* **1993**, *11*, 2174.
30. J. S. Corneille, J.-W. He, D. W. Goodman, *Surf. Sci.* **1994**, *306*, 269.
31. X. Xu, W. S. Oh, D. W. Goodman, *Langmuir* **1996**, *12*, 4877.
32. J. Guenster, G. Liu, V. Kempter, D. W. Goodman, *Surf. Sci.* **1998**, *415*, 303.
33. A. Kolmakov, J. Stultz, D. W. Goodman; *J. Chem. Phys.* **2000**, *113*, 7564.
34. Y. D. Kim, J. Stultz, T. Wei, D. W. Goodman, *J. Phys. Chem. B* **2002**, *106*, 6827.
35. Y. D. Kim, J. Stultz, D. W. Goodman, *Langmuir* **2002**, *18*, 3999.
36. Y. D. Kim, J. Stultz, D. W. Goodman, *Surf. Sci.* **2002**, *506*, 228.
37. Y. D. Kim, J. Stultz, T. Wei, D. W. Goodman, *J. Phys. Chem. B* **2003**, *107*, 592.
38. S. Wendt, Y. D. Kim, D. W. Goodman, *Prog. Surf. Sci.* **2003**, *74*, 141.
39. P. Audibert, M. Sidoumou, J. Suzanne, *Surf. Sci.* **1992**, *273*, L467.
40. R. Gerlach, A. Glebov, G. Lange, J. P. Toennies, H. Weiss, *Surf. Sci.* **1995**, *331–333*, 1490.
41. J. Heidberg, M. Kandel, D. Meine, U. Wildt, *Surf. Sci.* **1995**, *331–333*, 1467.
42. R. Wichtendahl, M. Rodriguez-Rodrigo, U. Härtel, H. Kuhlenbeck, H.-J. Freund, *Surf. Sci.* **1999**, *423*, 90.
43. G. Spoto, E. N. Gribov, G. Ricchiardi, A. Damin, D. Scarano, S. Bordiga, C. Lamberti, A. Zecchina, *Prog. Surf. Sci.* **2004**, *76*, 71.
44. Z. Dohnalek, G. A. Kimmel, S. A. Joyce, P. Ayotte, R. S. Smith, B. D. Kay, *J. Phys. Chem. B 105*, 3747.
45. G. Pacchioni, *Surf. Rev. Lett.* **2000**, *7*, 277.
46. G. Pacchioni, G. Cogliandro, P. S. Bagus, *Surf. Sci.* **1991**, *255*, 344.
47. G. Pacchioni, T. Minerva, P. S. Bagus, *Surf. Sci.* **1992**, *275*, 450.
48. G. Spoto, E. Gribov, A. Damin, G. Ricchiardi, A. Zecchina, *Surf. Sci.* **2003**, *540*, L605.
49. M. Sterrer, T. Risse, H.-J. Freund, *Surf. Sci.* **2005**, *596*, 222.
50. L. T. Steven, D. Zdenek, T. C. Charles, D. K. Bruce, *J. Chem. Phys.* **2005**, *122*, 164707.
51. L. T. Steven, D. Zdenek, T. C. Charles, D. K. Bruce, *J. Chem. Phys.* **2005**, *122*, 164708.
52. M. Yulikov, M. Sterrer, M. Heyde, H.-P. Rust, T. Risse, H. J. Freund, G. Pacchioni, A. Scagnelli, *Phys. Rev. Lett.* **2006**, *96*, 146804.
53. M. Sterrer, N. Nilius, M. Heyde, H.-P. Rust, T. Risse, H. J. Freund, private communication
54. A. Del Vitto, G. Pacchioni, F. Delbecq, P. Sautet, *J. Phys. Chem.* **2005**, *109*, 8040.
55. M. Sterrer, M. Yulikov, E. Fischbach, M. Heyde, H.-P. Rust, G. Pacchioni, T. Risse, H. J. Freund, *Angew. Chem. Int. Ed.* **2006**, *45*, 2630.
56. M. Sterrer, M. Yulikov, T. Risse, H. J. Freund, J. Carrasco, F. Illas, C. Di Valentin, L. Giordano, G. Pacchioni, *Angew. Chem. Int. Ed.* **2006**, *45*, 2633.
57. S. Abbet, A. Sanchez, U. Heiz, W. D. Schneider, A. M. Ferrari, G. Pacchioni, N. Rosch, *J. Am. Chem. Soc.* **2000**, *122*, 3453.

58. K. Judai, A. S. Worz, S. Abbet, J. M. Antonietti, U. Heiz, A. Del Vitto, L. Giordano, G. Pacchioni, *Phys. Chem. Chem. Phys.* **2005**, *7*, 955.
59. S. Abbet, U. Heiz, H. Hakkinen, U. Landman, *Phys. Rev. Lett.* **2001**, *86*, 5950.
60. J. M. Antonietti, M. Michalski, U. Heiz, H. Jones, K. H. Lim, N. Rosch, A. Del Vitto, G. Pacchioni, *Phys. Rev. Lett.* **2005**, *94*, 213402.
61. U. Heiz, W.-D. Schneider, *J. Phys. D: Appl. Phys.* **2000**, *33*, R85.
62. C. T. Campbell, *Curr. Opin. Solid State Mater. Sci.* **1998**, *3*, 439.
63. C. T. Campbell, A. W. Grant, D. E. Starr, S. C. Parker, V. A. Bondzie, *Top. Catal.* **2000**, *14*, 43.
64. C. T. Campbell, D. Starr, *J. Am. Chem. Soc.* **2002**, *124*, 9212.
65. J. T. Ranney, D. Starr, J. E. Musgrove, D. J. Bald, C. T. Campbell, *Faraday Disc.* **1999**, *114*, 195.
66. D. Starr, D. J. Bald, J. E. Musgrove, J. T. Ranney, C. T. Campbell, *J. Chem. Phys.* **2001**, *114*, 3752.
67. D. E. Starr, C. T. Campbell, *J. Phys. Chem. B* **2001**, *105*, 3776.
68. D. E. Starr, S. F. Diaz, J. E. Musgrove, J. T. Ranney, D. J. Bald, L. Nelen, H. Ihm, C. T. Campbell, *Surf. Sci.* **2002**, *515*, 13.
69. J. H. Larsen, J. T. Ranney, D. E. Starr, J. E. Musgrove, C. T. Campbell, *Phys. Rev. B* **2001**, *63*, 195410.
70. L. Xu, G. Henkelman, C. T. Campbell, H. Jonsson, *Surf. Sci.* **2006**, *600*, 1351.
71. X. Lijun, H. Graeme, T. C. Charles, J. Hannes, *Phys. Rev. Lett.* **2005**, *95*, 146103.
72. S. L. Tait, Z. Donalek, C. T. Campbell, B. D. Kay, *Surf. Sci.* **2005**, *591*, 90.
73. M. Valden, X. Lai, D. W. Goodman, *Science* **1998**, *281*, 1647.
74. R. Meyer, C. Lemire, S. Shaikhutdinov, H.-J. Freund, *Gold Bulletin* **2004**, *37*, 72.
75. S. Kielbassa, M. Kinne, R. J. Behm, *J. Phys. Chem. B* **2004**, *108*, 19184.
76. A. Maennig, Z. Zhao, D. Rosenthal, K. Christmann, H. Hoster, H. Rauscher, R. J. Behm, *Surf. Sci.* **2005**, *576*, 29.
77. M. S. Chen, D. W. Goodman, *Science* **2004**, *306*, 252.
78. C. Tegenkamp, H. Pfnuer, W. Ernst, U. Malaske, J. Wollschlaeger, D. Peterka, K. M. Schröder, V. Zielasek, M. Henzler, *J. Phys.: Condens. Matter* **1999**, *11*, 9943.
79. J. Kramer, W. Ernst, C. Tegenkamp, H. Pfnuer, *Surf. Sci.* **2002**, *517*, 87.
80. M. Sterrer, E. Fischbach, T. Risse, H.-J. Freund, *Phys. Rev. Lett.* **2005**, *94*, 186101.
81. M. Sterrer, E. Fischbach, M. Heyde, N. Nilius, H.-P. Rust, T. Risse, H. J. Freund, *J. Phys. Chem. B* **2006**, *110*, 8665.
82. C. Giovanardi, A. di Bona, T. S. Moia, S. Valeri, C. Pisani, M. Sgroi, M. Busso, *Surf. Sci.* **2002**, *505*, L209.
83. S. Valeri, S. Altieri, U. del Pennino, A. di Bona, P. Luches, A. Rota, *Phys. Rev. B* **2002**, *65*, 245410.
84. S. Schintke, S. Messerli, M. Pivetta, F. Patthey, L. Libioulle, M. Stengel, A. De Vita, W.-D. Schneider, *Phys. Rev. Lett.* **2001**, *87*, 276801.
85. R. Wichtendahl, M. Rodrigez-Rodrigo, U. Härtel, H. Kuhlenbeck, H. J. Freund, *Phys. Stat. Sol. A* **1999**, *173*, 93.
86. G. Pacchioni, *Chemphyschem* **2003**, *4*, 1041.
87. E. Giamello, M. C. Paganini, D. M. Murphy, A. M. Ferrari, G. Pacchioni, *J. Phys. Chem. B* **1997**, *101*, 971.
88. M. Chiesa, M. C. Paganini, G. Spoto, A. Del Vitto, C. Di Valentin, G. Pacchioni, E. Giamello, *J. Phys. Chem. B* **2005**, *109*, 7314.
89. T. Berger, M. Sterrer, O. Diwald, E. Knoezinger, *J. Phys. Chem. B* **2004**, *108*, 7280.
90. S. K. Purnell, X. Xu, D. W. Goodman, B. C. Gates, *J. Phys. Chem.* **1994**, *98*, 4076.
91. S. K. Purnell, X. Xu, D. W. Goodman, B. C. Gates, *Langmuir* **1994**, *10*, 3057.
92. H. Kuhlenbeck, G. Odorfer, R. Jaeger, C. Xu, T. Mull, B. Baumeister, G. Illing, M. Menges, H. J. Freund, D. Weide, *Vacuum* **1990**, *41*, 34.
93. H. Kuhlenbeck, G. Odörfer, R. Jaeger, G. Illing, M. Menges, T. Mull, H.-J. Freund, M. Pöhlchen, V. Staemmler, S. Witzel, C. Scharfschwerdt, K. Wennemann, T. Liedtke, M. Neumann, *Phys. Rev. B* **1991**, *43*, 1969.
94. M. Bäumer, D. Cappus, H. Kuhlenbeck, H. J. Freund, G. Wilhelmi, A. Brodde, H. Neddermeye, *Surf. Sci.* **1991**, *253*, 116.
95. T. Mull, B. Baumeister, M. Menges, H.-J. Freund, D. Weide, C. Fischer, P. Andresen, *J. Chem. Phys.* **1992**, *96*, 7108.
96. M. Bäumer, D. Cappus, G. Illing, H. Kuhlenbeck, H. J. Freund, *J. Vac. Sci. Technol. A – Vacuum Surfaces & Films* **1992**, *10*, 2407.
97. A. Freitag, V. Staemmler, D. Cappus, C. A. Ventrice Jr., K. Al-Shamery, H. Kuhlenbeck, H.-J. Freund, *Chem. Phys. Lett.* **1993**, *210*, 10.
98. D. Cappus, C. Xu, D. Ehrlich, B. Dillmann, J. Ventrice, C. A. K. Al Shamery, H. Kuhlenbeck, H.-J. Freund, *Chem. Phys.* **1993**, *177*, 533.
99. D. Cappus, M. Menges, C. Xu, D. Ehrlich, B. Dillmann, J. C. A. Ventrice, J. Libuda, M. Bäumer, S. Wohlrab, *J. Elect. Spect. Rel. Phenom.* **1994**, *68*, 347.
100. S. D. Peacor, T. Hibma, *Surf. Sci.* **1994**, *301*, 11.
101. C. Lamberti, E. Groppo, C. Prestipino, S. Casassa, A. M. Ferrari, C. Pisani, C. Giovanardi, P. Luches, S. Valeri, F. Boscherini, *Phys. Rev. Lett.* **2003**, *91*, 046101.
102. G. Pacchioni, C. D. Valentin, D. Dominguez-Ariza, F. Illas, T. Bredow, T. Kluener, V. Staemmler, *J. Phys. Cond. Matter* **2004**, *16*, S2497.
103. J. T. Hoeft, M. Kittel, M. Polcik, S. Bao, R. L. Toomes, J. H. Kang, D. P. Woodruff, M. Pascal, C. L. A. Lamont, *Phys. Rev. Lett.* **2001**, *87*, 086101.
104. M. Kittel, J. T. Hoeft, S. Bao, M. Polcik, R. L. Toomes, J. H. Kang, D. P. Woodruff, M. Pascal, C. L. A. Lamont, *Surf. Sci.* **2002**, *499*, 1.
105. M. Menges, B. Baumeister, K. Al-Shamery, H.-J. Freund, C. Fischer, P. Andresen, *J. Chem. Phys.* **1994**, *101*(4), 3318.
106. M. Menges, B. Baumeister, K. Al-Shamery, H.-J. Freund, C. Fischer, P. Andresen, *Surf. Sci.* **1994**, *316*, 103.
107. T. Klüner, H.-J. Freund, J. Freitag, V. Staemmler, *J. Chem. Phys.* **1996**, *104*, 10030.
108. F. Budde, A. V. Hamza, P. M. Ferm, G. Ertl, D. Weide, P. Andresen, H.-J. Freund, *Phys. Rev. Lett.* **1988**, *60*, 1518.
109. T. Klüner, H.-J. Freund, V. Staemmler, R. Kosloff, *Phys. Rev. Lett.* **1998**, *80*, 5208.
110. C. Bach, T. Klüner, A. Gro, *Chem. Phys. Lett.* **2003**, *376*, 424.
111. S. Dittrich, H. J. Freund, C. P. Koch, R. Kosloff, T. Klüner, *J. Chem. Phys.* **2006**, *124*, 024702.
112. I. Mehdaoui, D. Kröner, M. Pykavy, H. J. Freund, T. Klüner, *Phys. Chem. Chem. Phys.* **2006**, *8*, 1584.
113. C. M. Truong, M.-C. Wu, D. W. Goodman, *J. Chem. Phys.* **1992**, *97*, 9447.
114. M. C. Wu, C. M. Truong, D. W. Goodman, *J. Phys. Chem.* **1993**, *97*, 4182.
115. C. M. Truong, M. C. Wu, D. W. Goodman, *J. Am. Chem. Soc.* **1993**, *115*, 3647.

116. M. C. Wu, C. M. Truong, D. W. Goodman, *J. Phys. Chem.* **1993**, *97*, 9425.
117. M. C. Wu, C. M. Truong, D. W. Goodman, *J. Phys. Chem.* **1993**, *97*, 4182.
118. S. M. Vesecky, X. P. Xu, D. W. Goodman, *J. Vac. Sci. Technol., A* **1994**, *12*, 2114.
119. F. Rohr, K. Wirth, J. Libuda, D. Cappus, M. Bäumer, H.-J. Freund, *Surf. Sci.* **1994**, *315*, L977.
120. F. Winkelmann, S. Wohlrab, J. Libuda, M. Bäumer, D. Cappus, M. Menges, K. Al-Shamery, H. Kuhlenbeck, H. J. Freund, *Surf. Sci.* **1994**, *307–309*, 1148.
121. M. Schönnenbeck, D. Cappus, J. Klinkmann, H.-J. Freund, L. G. M. Petterson, P. S. Bagus, *Surf. Sci.* **1996**, *347*, 337.
122. A. Bandara, J. Kobota, A. Wada, K. Domen, C. Hirose, *Surf. Sci. Lett.* **1996**, *364*, L 580.
123. A. Bandara, J. Kubota, A. Wada, K. Domen, C. Hirose, *J. Phys. Chem.* **1996**, *100*, 14962.
124. A. Bandara, J. Kubota, A. Wada, K. Domen, C. Hirose, *J. Phys. Chem. B* **1997**, *101*, 361.
125. J. Kubota, A. Bandara, A. Wada, K. Domen, C. Hirose, *Surf. Sci.* **1996**, *368*, 361.
126. D. Cappus, M. Hassel, E. Neuhaus, M. Heber, F. Rohr, H. J. Freund, *Surf. Sci.* **1995**, *337*, 268.
127. M. Hassel, H.-J. Freund, *Surf. Sci.* **1995**, *325*, 163.
128. M. Hassel, H. Kuhlenbeck, H.-J. Freund, S. Shi, A. Freitag, V. Staemmler, S. Lutkehoff, M. Neumann, *Chem. Phys. Lett.* **1995**, *240*, 205.
129. M. Hassel, H. J. Freund, *Surf. Sci. Spectra* **1998**, *4*, 273.
130. R. M. Jaeger, H. Kuhlenbeck, H.-J. Freund, M. Wuttig, W. Hoffmann, R. Franchy, H. Ibach, *Surf. Sci.* **1991**, *259*, 235.
131. J. Libuda, F. Winkelmann, M. Bäumer, H.-J. Freund, T. Bertrams, H. Neddermeyer, K. Müller, *Surf. Sci.* **1994**, *318*, 61.
132. H. Niehus, *Nucl. Instrum. Methods Phys. Res., Sect. B* **1988**, *33*, 876.
133. R.-P. Blum, D. Ahlbehrendt, H. Niehus, *Surf. Sci.* **1998**, *396*, 176.
134. C. Becker, J. Kandler, H. Raaf, R. Linke, T. Pelster, M. Dräger, M. Tanemura, K. Wandelt, *J. Vac. Sci. Technol. A* **1998**, *16*, 1000.
135. A. Rosenhahn, J. Schneider, C. Becker, K. Wandelt, *J. Vac. Sci. Technol. A* **2000**, *18*, 1923.
136. A. Rosenhahn, J. Schneider, J. Kandler, C. Becker, K. Wandelt, *Surf. Sci.* **1999**, *433–435*, 705.
137. G. Ceballos, Z. Song, J. I. Pascual, H. P. Rust, H. Conrad, M. Bäumer, H. J. Freund, *Chem. Phys. Lett.* **2002**, *359*, 41.
138. M. Kulawik, N. Nilius, H.-P. Rust, H.-J. Freund, *Phys. Rev. Lett.* **2003**, *91*, 256101.
139. G. Kresse, M. Schmid, E. Napetschnig, M. Shishkin, L. Köhler, P. Varga, *Science* **2005**, *308*, 1440.
140. R. M. Jaeger, K. Homann, H. Kuhlenbeck, H.-J. Freund, *Chem. Phys. Lett.* **1993**, *203*, 41.
141. S. Schauermann, V. Johanek, M. Laurin, J. Libuda, H. J. Freund, *Chem. Phys. Lett.* **2003**, *381*, 298.
142. S. Schauermann, V. Johanek, M. Laurin, J. Libuda, H. J. Freund, *Phys. Chem. Chem. Phys.* **2003**, *5*, 5139.
143. M. Bäumer, J. Libuda, A. Sandell, H.-J. Freund, G. Graw, T. Bertrams, H. Neddermeyer, *Ber. Bunsenges. Phys. Chem.* **1995**, *99*, 1381.
144. M. Klimenkov, S. Nepijko, H. Kuhlenbeck, H.-J. Freund, *Surf. Sci.* **1997**, *385*, 66.
145. M. Klimenkov, S. Nepijko, H. Kuhlenbeck, M. Bäumer, R. Schlögl, H.-J. Freund, *Surf. Sci.* **1997**, *391*, 27.
146. S. A. Nepijko, M. Klimenkov, H. Kuhlenbeck, H.-J. Freund, *J. Vac. Sci. Technol., A* **1999**, *17*, 577.
147. H. J. Freund, B. Dillmann, D. Ehrlich, M. Hassel, R. M. Jaeger, H. Kuhlenbeck, C. A. Ventrice Jr., F. Winkelmann, S. Wohlrab, C. Xu, T. Bertrams, A. Brodde, H. Neddermeyer, *J. Mol. Catal.* **1993**, *82*, 143.
148. D. R. Mullins, S. H. Overbury, *Surf. Sci.* **2002**, *511*, L293.
149. J. Libuda, M. Frank, A. Sandell, S. Andersson, P. A. Brühwiler, M. Baeumer, N. Martensson, H. J. Freund, in *Elementary Processes in Excitations and Reactions on Solid Surfaces*, Vol. 121, A. Okiji, H. Kasai, K. Makoshi (Eds.), Springer, Berlin, 1996, p. 210.
150. S. Stempel, M. Bäumer, H. J. Freund, *Surf. Sci.* **1998**, *402–404*, 424.
151. J. T. Yates, E. D. Williams, W. H. Weinberg, *Surf. Sci.* **1980**, *91*, 562.
152. V. Matolin, M. H. Elyakhloufi, K. Masek, E. Gillet, *Catal. Lett.* **1993**, *21*, 175.
153. V. Matolin, K. Masek, M. H. Elyakhloufi, E. Gillet, *J. Catal.* **1993**, *143*, 492.
154. V. Nehasil, I. Stara, V. Matolin, *Surf. Sci.* **1995**, *331–333*, 105.
155. M. Frank, S. Andersson, J. Libuda, S. Stempel, A. Sandell, B. Brena, A. Giertz, P. A. Bruhwiler, M. Bäumer, N. Martensson, H. J. Freund, *Chem. Phys. Lett.* **1997**, *279*, 92.
156. M. Frank, S. Andersson, J. Libuda, S. Stempel, A. Sandell, B. Brena, A. Giertz, P. A. Brühwiler, M. Baeumer, N. Martensson, H. J. Freund, *Chem. Phys. Lett.* **1999**, *310*, 229.
157. R. A. Marbrow, R. M. Lambert, *Surf. Sci.* **1977**, *67*, 489.
158. M. Rebholz, R. Prins, N. Kruse, *Surf. Sci.* **1991**, *259*, L797.
159. H. J. Freund, N. Ernst, M. Baeumer, G. Rupprechter, J. Libuda, H. Kuhlenbeck, T. Risse, W. Drachsel, K. Al Shamery, H. Hamann, in *Surface Chemistry and Catalysis*, A. F. Carley, P. R. Davies, G. J. Hutchings, M. S. Spencer (Eds.), Kluwer, New York, 2002, pp. 103.
160. K. H. Hansen, T. Worren, S. Stempel, E. Lægsgaard, M. Baeumer, H. J. Freund, F. Besenbacher, I. Stensgaard, *Phys. Rev. Lett.* **1999**, *83*, 4120.
161. N. Nilius, T. M. Wallis, W. Ho, *Phys. Rev. Lett.* **2003**, *90*, 046808.
162. M. Heemeier, A. F. Carlsson, M. Naschitzki, M. Schmal, M. Baeumer, H. J. Freund, *Angew. Chem. Int. Ed.* **2002**, *41*, 4073.
163. A. F. Carlsson, M. Naschitzki, M. Bäumer, H. J. Freund, *J. Phys. Chem. B* **2003**, *107*, 778.
164. T. Risse, A. Carlsson, M. Baeumer, T. Klüner, H. J. Freund, *Surf. Sci.* **2003**, *546*, L829.
165. A. F. Carlsson, M. Bäumer, T. Risse, H. J. Freund, *J. Chem. Phys.* **2003**, *119*, 10885.
166. N. A. Khan, A. Uhl, S. Shaikhutdinov, H. J. Freund, *Surf. Sci.* **2006**, *600*, 1849.
167. N. A. Khan, S. Shaikhutdinov, H. Freund, *Catal. Lett.* **2006**, *108*, 159.
168. G. Rupprechter, H. J. Freund, *Top. Catal.* **2000**, *14*, 3.
169. G. Rupprechter, T. Dellwig, H. Unterhalt, H.-J. Freund, *J. Phys. Chem. B* **2001**, *105*, 3797.
170. T. Dellwig, J. Hartmann, J. Libuda, I. Meusel, G. Rupprechter, H. Unterhalt, H.-J. Freund, *J. Mol. Catal. A* **2000**, *162*, 51.
171. T. Dellwig, G. Rupprechter, H. Unterhalt, H.-J. Freund, *Phys. Rev. Lett.* **2000**, *85*, 776.
172. G. Rupprechter, T. Dellwig, H. Unterhalt, H.-J. Freund, *Top. Catal.* **2001**, *15*, 19.
173. H. Unterhalt, G. Rupprechter, H. J. Freund, *J. Phys. Chem. B* **2002**, *106*, 356.

174. H.-J. Freund, M. Bäumer, J. Libuda, T. Risse, G. Rupprechter, S. Shaikhutdinov, *J. Catal.* **2003**, *216*, 223.
175. I. V. Yudanov, R. Sahnoun, K. M. Neyman, N. Rosch, J. Hoffmann, S. Schauermann, V. Johanek, H. Unterhalt, G. Rupprechter, J. Libuda, H. J. Freund, *J. Phys. Chem. B* **2003**, *107*, 255.
176. M. Morkel, G. Rupprechter, H.-J. Freund, *Surf. Sci.* **2005**, *588*, L209.
177. J. Silvestre-Albero, G. Rupprechter, H.-J. Freund, *Chem. Commun.* **2006**, 80.
178. M. Borasio, O. Rodrigez de la Fuente, G. Rupprechter, H.-J. Freund, *J. Phys. Chem. B* **2005**, *109*, 17791.
179. O. Rodriguez de la Fuente, M. Borasio, P. Galletto, G. Rupprechter, H.-J. Freund, *Surf. Sci.* **2004**, *566–568*, 740.
180. S. Schauermann, J. Hoffmann, V. Johanek, J. Hartmann, J. Libuda, H.-J. Freund, *Angew. Chem. Int. Ed.* **2002**, *41*, 2532.
181. V. V. Kaichev, I. P. Prosvirin, V. I. Bukhtiyarov, H. Unterhalt, G. Rupprechter, H.-J. Freund, *J. Phys. Chem. B* **2003**, *107*, 3522.
182. D. L. Doering, H. Poppa, J. T. Dickinson, *J. Catal.* **1982**, *73*, 104.
183. D. R. Rainer, C. Xu, P. M. Holmblad, D. W. Goodman, *J. Vac. Sci. Technol. A* **1997**, *15*, 1653.
184. V. Johanek, S. Schauermann, M. Laurin, J. Libuda, H.-J. Freund, *Angew. Chem. Int. Ed.* **2003**, *42*, 3035.
185. N. Nilius, N. Ernst, H.-J. Freund, *Phys. Rev. Lett.* **2000**, *84*, 3994.
186. H. M. Benia, N. Nilius, H.-J. Freund, *Surf. Sci.* **2007**, *601*, L55.
187. W. Benten, N. Nilius, N. Ernst, H.-J. Freund, *Phys. Rev. B* **2005**, *72*, 045403.
188. N. Nilius, N. Ernst, H.-J. Freund, *Surf. Sci.* **2001**, *478*, L327.
189. C. Winkler, A. Carew, R. Raval, J. Ledieu, R. McGrath, *Surf. Rev. Lett.* **2001**, *8*, 693.
190. N. Nilius, N. Ernst, H.-J. Freund, *Phys. Rev. B* **2002**, *65*, 115421.
191. S. K. Shaikhutdinov, R. Meyer, M. Naschitzki, M. Baeumer, H.-J. Freund, *Catal. Lett.* **2003**, *86*, 211.
192. A. M. Doyle, S. Shaikhutdinov, H.-J. Freund, *J. Catal.* **2004**, *223*, 444.
193. S. Shaikhutdinov, M. Frank, M. Bäumer, S. D. Jackson, R. J. Oldman, J. C. Hemminger, H.-J. Freund, *Catal. Lett.* **2002**, *80*, 125.
194. A. M. Doyle, S. Shaikhutdinov, S. D. Jackson, H.-J. Freund, *Angew. Chem., Int. Ed.* **2003**, *42*, 5240.
195. A. M. Doyle, S. Shaikhutdinov, H.-J. Freund, *Angew. Chem. Int. Ed.* **2005**, *44*, 629.
196. J. Silvestre-Albero, G. Rupprechter, H.-J. Freund, *J. Catal.* **2005**, *235*, 52.
197. J. Silvestre-Albero, G. Rupprechter, H.-J. Freund, *J. Catal.* **2006**, *240*, 58.
198. J. Libuda, M. Frank, A. Sandell, S. Andersson, P. A. Brühwiler, M. Bäumer, N. Mårtensson, H.-J. Freund, *Surf. Sci.* **1997**, *384*, 106.
199. M. Heemeier, M. Frank, J. Libuda, K. Wolter, H. Kuhlenbeck, M. Bäumer, H.-J. Freund, *Catal. Lett.* **2000**, *68*, 19.
200. M. Heemeier, S. Stempel, S. K. Shaikhutdinov, J. Libuda, M. Bäumer, R. J. Oldman, S. D. Jackson, H.-J. Freund, *Surf. Sci.* **2003**, *523*, 103.
201. G. Pacchioni, L. Giordano, M. Baistrocchi, *Phys. Rev. Lett.* **2005**, *94*, 226104.
202. N. F. Mott, *Trans. Faraday Soc.* **1947**, *43*, 429.
203. M. Kulawik, N. Nilius, H.-J. Freund, *Phys. Rev. Lett.* **2006**, *96*, 036103.
204. N. Magg, J. B. Giorgi, T. Schroeder, M. Bäumer, H.-J. Freund, *J. Phys. Chem. B* **2002**, *106*, 8756.
205. N. Magg, J. B. Giorgi, A. Hammoudeh, T. Schroeder, M. Bäumer, H.-J. Freund, *J. Phys. Chem. B* **2003**, *107*, 9003.
206. N. Magg, B. Immaraporn, J. Giorgi, T. Schroeder, M. Bäumer, J. Döbler, Z. Wu, E. Kondratenko, M. Cherian, M. Baerns, P. C. Stair, J. Sauer, H.-J. Freund, *J. Catal.* **2004**, *226*, 88.
207. N. Magg, J. Giorgi, M. Frank, B. Immaraporn, T. Schroeder, M. Baeumer, H.-J. Freund, *J. Am. Chem. Soc.* **2004**, *126*, 3613.
208. S. Guimond, M. Abu Haija, S. Kaya, J. Lu, J. Weissenrieder, S. Shaikhutdinov, H. Kuhlenbeck, H.-J. Freund, J. Döbler, J. Sauer, *Top. Catal.* **2006**, *38*, 117.
209. J. Sauer, J. Döbler, *Dalton Trans.* **2004**, 3116.
210. S. G. Addepalli, B. Ekstrom, N. P. Magtoto, J. S. Lin, J. A. Kelber, *Surf. Sci.* **1999**, *442*, 385.
211. N. P. Magtoto, C. Niu, M. Anzaldua, J. A. Kelber, D. R. Jennison, *Surf. Sci.* **2001**, *472*, L157.
212. C. Niu, K. Shepherd, D. Martini, J. Tong, J. A. Kelber, D. R. Jennison, A. Bogicevic, *Surf. Sci.* **2000**, *465*, 163.
213. M. Garza, N. P. Magtoto, J. A. Kelber, *Surf. Sci.* **2002**, *519*, 259.
214. C. Becker, A. Rosenhahn, A. Wiltner, K. von Bergmann, J. Schneider, P. Pervan, M. Milun, K. Wandelt, *New J. Phys.* **2002**, *4*, 75.1.
215. P. J. Chen, D. W. Goodman, *Surf. Sci.* **1994**, *312*, L767.
216. M. C. Wu, D. W. Goodman, *J. Phys. Chem.* **1994**, *98*, 9874.
217. H. Poppa, *Catal. Rev. Sci. Eng.* **1993**, *35*, 359.
218. H. Poppa, *Vacuum* **1984**, *34*, 1081.
219. H. Poppa, *Ultramicroscopy* **1983**, *11*, 105.
220. X. Xu, D. W. Goodman, *Appl. Phys. Lett.* **1992**, *61*, 774.
221. X. Xu, D. W. Goodman, *Surf. Sci.* **1993**, *282*, 323.
222. L. E. Davis, N. C. MacDonald, P. W. Palmberg, G. E. Riach, R. E. Weber, *Handbook of Auger Electron Spectroscopy*, Eden Prairie, Minn.: Phys. Electr. Div., Perkin-Elmer Co., 1976.
223. B. A. Joyce, J. H. Neave, *Surf. Sci.* **1971**, *27*, 499.
224. C. S. Ko, R. J. Gorte, *Surf. Sci.* **1985**, *155*, 296.
225. J. Derrien, M. Commandre, *Surf. Sci.* **1982**, *118*, 32.
226. W. Braun, H. Kuhlenbeck, *Surf. Sci.* **1987**, *180*, 279.
227. A. Bianconi, R. S. Bauer, *Surf. Sci.* **1980**, *99*, 76.
228. N. Lieske, R. Hezel, *Thin Solid Films* **1979**, *61*, 217.
229. T. Schröder, M. Adelt, B. Richter, M. Naschitzki, M. Bäumer, H.-J. Freund, *Surf. Rev. Lett.* **2000**, *7*, 7.
230. T. Schröder, M. Adelt, B. Richter, M. Naschitzki, M. Bäumer, H.-J. Freund, *Microelectronics Reliability* **2000**, *40*, 841.
231. T. Schröder, A. Hammoudeh, M. Pykavy, N. Magg, M. Adelt, M. Bäumer, H.-J. Freund, *Solid-State Electron.* **2001**, *45*, 1471.
232. T. Schröder, J. Giorgi, M. Bäumer, H.-J. Freund, *Phys. Rev. B* **2002**, *66*, 165422.
233. M. S. Chen, A. K. Santra, D. W. Goodman, *Phys. Rev. B* **2004**, *69*, 155404.
234. S. Wendt, E. Ozensoy, T. Wei, M. Frerichs, Y. Cai, M. S. Chen, D. W. Goodman, *Phys. Rev. B* **2005**, *72*, 115409.
235. M. S. Chen, A. K. Santra, D. W. Goodman, *J. Phys. Chem. B* **2004**, *108*, 17940.
236. J. Weissenrieder, S. Kaya, J.-L. Lu, H.-J. Gao, S. Shaikhutdinov, H.-J. Freund, M. Sierka, T. K. Todorova, J. Sauer, *Phys. Rev. Lett.* **2005**, *95*, 076103.
237. X. P. Xu, S. M. Vesecky, D. W. Goodman, *Science* **1992**, *258*, 788.
238. X. Xu, J.-W. He, D. W. Goodman, *Surf. Sci.* **1993**, *284*, 103.
239. X. Xu, D. W. Goodman, *J. Phys. Chem.* **1993**, *97*, 683.
240. J. Szanyi, W. K. Kuhn, D. W. Goodman, *J. Phys. Chem.* **1994**, *98*, 2978.

241. J. Szanyi, D. W. Goodman, *J. Phys. Chem.* **1994**, *98*, 2972.
242. X. Xu, D. W. Goodman, *J. Phys. Chem.* **1993**, *97*, 7711.
243. X. Xu, D. W. Goodman, *Catal. Lett.* **1994**, *24*, 31.
244. P. W. Davies, R. M. Lambert, *Surf. Sci.* **1981**, *110*, 227.
245. H. D. Schmick, H. W. Wassmuth, *Surf. Sci.* **1982**, *123*, 471.
246. S. W. Jorgensen, N. D. S. Canning, R. J. Madix, *Surf. Sci.* **1987**, *179*, 322.
247. D. T. Wickham, B. A. Banse, B. E. Koel, *Surf. Sci.* **1991**, *243*, 83.
248. W. T. Wallace, B. K. Min, D. W. Goodman, *J. Molec. Catal. A: Chemical* **2005**, *228*, 3.
249. B. K. Min, W. T. Wallace, D. W. Goodman, *J. Phys. Chem. B* **2004**, *108*, 14609.
250. W. S. Oh, C. Xu, D. Y. Kim, D. W. Goodman, *J. Vac. Sci. Technol., A* **1997**, *15*, 1710.
251. Q. Guo, W. S. Oh, D. W. Goodman, *Surf. Sci.* **1999**, *437*, 49.
252. X. Lai, Q. Guo, B. K. Min, D. W. Goodman, *Surf. Sci.* **2001**, *487*, 1.
253. A. B. Boffa, H. C. Galloway, P. W. Jacobs, J. J. Benitez, J. D. Batteas, M. Salmeron, A. T. Bell, G. A. Somorjai, *Surf. Sci.* **1995**, *326*, 80.
254. T. V. Ashworth, G. Thornton, *Thin Solid Films* **2001**, *400*, 43.
255. Z. Chang, G. Thornton, *Surf. Sci.* **2000**, *462*, 68.
256. N. D. McCavish, R. A. Bennett, *Surf. Sci.* **2003**, *546*, 47.
257. M. S. Chen, W. T. Wallace, D. Kumar, Z. Yan, K. K. Gath, Y. Cai, Y. Kuroda, D. W. Goodman, *Surf. Sci.* **2005**, *581*, 115.
258. D. W. Goodman, *Catal. Lett.* **2005**, *99*, 1.
259. M. S. Chen, K. Luo, D. Kumar, W. T. Wallace, C. W. Yi, K. K. Gath, D. W. Goodman, *Surf. Sci.* **2007**, *601*, 632.
260. C. T. Campbell, *Science* **2004**, *306*, 234.
261. C. Xu, M. Hassel, H. Kuhlenbeck, H.-J. Freund, *Surf. Sci.* **1991**, *258*, 23.
262. C. Xu, B. Dillmann, H. Kuhlenbeck, H.-J. Freund, *Phys. Rev. Lett.* **1991**, *67*, 3551.
263. H. Kuhlenbeck, C. Xu, B. Dillmann, M. Hassel, B. Adam, D. Ehrlich, S. Wohlrab, H.-J. Freund, U. A. Ditzinger, H. Neddermeyer, M. Neuber, M. Neumann, *Ber. Bunsen-Ges. Phys. Chem.* **1992**, *96*, 15.
264. C. A. Ventrice Jr., D. Ehrlich, E. L. Garfunkel, B. Dillmann, D. Heskett, H.-J. Freund, *Phys. Rev. B* **1992**, *46*, 12892.
265. K. Al-Shamery, I. Beauport, H.-J. Freund, H. Zacharias, *Chem. Phys. Lett.* **1994**, *222*, 107.
266. H. M. Kennett, A. E. Lee, *Surf. Sci.* **1972**, *33*, 377.
267. P. Michel, C. Jardin, *Surf. Sci.* **1973**, *36*, 478.
268. S. Ekelund, C. Leygraf, *Surf. Sci.* **1973**, *40*, 179.
269. F. Watari, J. M. Cowley, *Surf. Sci.* **1981**, *105*, 240.
270. B. Dillmann, F. Rohr, O. Seiferth, G. Klivenyi, M. Bender, K. Homann, I. N. Yakovkin, D. Ehrlich, M. Bäumer, H. Kuhlenbeck, H.-J. Freund, *Faraday Disc.* **1996**, *105*, 295.
271. I. Beauport, K. Al-Shamery, H.-J. Freund, *Chem. Phys. Lett.* **1996**, *256*, 641.
272. I. Beauport, K. Al-Shamery, H.-J. Freund, *Surf. Sci.* **1996**, *363*, 252.
273. M. Pykavy, V. Staemmler, O. Seiferth, H.-J. Freund, *Surf. Sci.* **2001**, *479*, 11.
274. S. Thiel, M. Pykavy, T. Klüner, H.-J. Freund, R. Kosloff, V. Staemmler, *Phys. Rev. Lett.* **2001**, *87*, 077601.
275. S. Thiel, T. Klüner, D. Lemoine, H.-J. Freund, *Chem. Phys.* **2002**, *282*, 361.
276. S. Thiel, M. Pykavy, T. Klüner, H.-J. Freund, R. Kosloff, V. Staemmler, *J. Chem. Phys.* **2002**, *116*, 762.
277. S. Borowski, T. Klüner, H.-J. Freund, I. Klinkmann, K. Al-Shamery, M. Pykavy, V. Staemmler, *Appl. Phys. A* **2004**, *78*, 223.
278. S. Borowski, T. Klüner, H.-J. Freund, *J. Chem. Phys.* **2003**, *119*, 10367.
279. M. Wilde, O. Seiferth, K. Al-Shamery, H.-J. Freund, *J. Chem. Phys.* **1999**, *111*, 1158.
280. M. Wilde, I. Beauport, F. Stuhl, K. Al-Shamery, H.-J. Freund, *Phys. Rev. B* **1999**, *59*, 13401.
281. K. B. Lewis, S. T. Oyama, G. A. Somorjai, *Surf. Sci.* **1990**, *233*, 75.
282. F. P. Leisenberger, S. Surnev, L. Vitali, M. G. Ramsey, F. P. Netzer, *J. Vac. Sci. Technol., A* **1999**, *17*, 1743.
283. L. Surnev, G. Kresse, J. A. Ramsey, F. P. Netzer, *Phys. Rev. Lett.* **2001**, *87*, 86102.
284. M. Sock, S. Surnev, M. G. Ramsey, F. P. Netzer, *Top. Catal.* **2000**, *14*, 15.
285. J. Schoiswohl, M. Sock, S. Surnev, M. G. Ramsey, F. P. Netzer, G. Kresse, J. N. Andersen, *Surf. Sci.* **2004**, *555*, 101.
286. A.-C. Dupuis, M. Abu Haija, B. Richter, H. Kuhlenbeck, H.-J. Freund, *Surf. Sci.* **2003**, *539*, 99.
287. M. Abu Haija, S. Guimond, Y. Romanyshyn, A. Uhl, H. Kuhlenbeck, T. K. Todorova, M. V. Ganduglia-Pirovano, J. Dobler, J. Sauer, H.-J. Freund, *Surf. Sci.* **2006**, *600*, 1497.
288. S. Guimond, H. Kuhlenbeck, M. Naschitzki, H.-J. Freund, private communication.
289. Y. Romanyshyn, H. Kuhlenbeck, H.-J. Freund, private communication.
290. W. Weiss, W. Ranke, *Prog. Surf. Sci.* **2002**, *70*, 1.
291. G. H. Vurens, M. Salmeron, G. A. Somorjai, *Surf. Sci.* **1988**, *201*, 129.
292. G. H. Vurens, V. Maurice, M. Salmeron, G. A. Somorjai, *Surf. Sci.* **1992**, *268*, 170.
293. H. C. Galloway, J. J. Benitez, M. Salmeron, *J. Vac. Sci. Technol., A* **1994**, *12*, 2302.
294. M. Ritter, W. Ranke, W. Weiss, *Phys. Rev. B* **1998**, *57*, 7240–7251.
295. S. Shaikhutdinov, M. Ritter, W. Weiss, *Phys. Rev. B* **2000**, *62*, 7535–7541.
296. Y. J. Kim, C. Westphal, R. X. Ynzunza, H. C. Galloway, M. Salmeron, M. A. Van Hove, C. S. Fadley, *Phys. Rev. B* **1997**, *55*, R13448–R13451.
297. X.-G. Wang, W. Weiss, S. K. Shaikhoutdinov, M. Ritter, M. Petersen, F. Wagner, R. Schlögl, M. Scheffler, *Phys. Rev. Lett.* **1998**, *81*, 1038.
298. S. K. Shaikhutdinov, W. Weiss, *Surf. Sci.* **1999**, *432*, L627.
299. S. A. Chambers, S. I. Yi, *Surf. Sci.* **1999**, *439*, L785.
300. G. Ketteler, W. Weiss, W. Ranke, *Surf. Rev. Lett.* **2001**, *8*, 661.
301. C. Lemire, S. Bertarione, A. Zecchina, D. Scarano, A. Chaka, S. Shaikhutdinov, H.-J. Freund, *Phys. Rev. Lett.* **2005**, *94*, 166101.
302. N. G. Condon, F. M. Leibsle, A. R. Lennie, P. W. Murray, D. J. Vaughan, G. Thornton, *Phys. Rev. Lett.* **1995**, *75*, 1961.
303. A. R. Lennie, N. G. Condon, F. M. Leibsle, P. W. Murray, G. Thornton, D. J. Vaughan, *Phys. Rev. B* **1996**, *53*, 10244–10253.
304. S. Shaikhutdinov, M. Ritter, X.-G. Wang, H. Over, W. Weiss, *Phys. Rev. B* **1999**, *60*, 11062–11069.
305. C. Lemire, R. Meyer, V. E. Henrich, S. Shaikhutdinov, H.-J. Freund, *Surf. Sci.* **2004**, *572*, 103.
306. S. Shaikhutdinov, R. Meyer, D. Lahav, M. Baeumer, T. Klüner, H.-J. Freund, *Phys. Rev. Lett.* **2003**, *91*, 076102.
307. C. Lemire, K. Meyer, S. Shaikhutdinov, H.-J. Freund, *Angew. Chem. Int. Ed.* **2003**, *43*, 118.
308. C. Lemire, R. Meyer, S. K. Shaikhutdinov, H.-J. Freund, *Surf. Sci.* **2004**, *552*, 27.

309. R. Meyer, D. Lahav, T. Schalow, M. Laurin, B. Brandt, S. Schauermann, S. Guimond, T. Klüner, H. Kuhlenbeck, J. Libuda, *Surf. Sci.* **2005**, *586*, 174.
310. N. Nilius, E. D. L. Rienks, H.-P. Rust, H.-J. Freund, *Phys. Rev. Lett.* **2005**, *95*, 066101.
311. T. Schalow, M. Laurin, B. Brandt, S. Schauermann, S. Guimond, H. Kuhlenbeck, D. E. Starr, S. Shaikhutdinov, J. Libuda, H.-J. Freund, *Angew. Chem. Int. Ed.* **2005**, *44*, 7601.
312. T. Schalow, B. Brandt, D. Starr, M. Laurin, S. Schauermann, S. Shaikhutdinov, J. Libuda, H.-J. Freund, *Catal. Lett.* **2006**, *107*, 189.
313. T. Schalow, B. Brandt, D. Starr, M. Laurin, S. Shaikhutdinov, J. Libuda, H.-J. Freund, *Angew. Chem. Int. Ed.* **2006**, *45*, 3693.
314. T. Schalow, B. Brandt, M. Laurin, S. Schauermann, S. Guimond, H. Kuhlenbeck, J. Libuda, H.-J. Freund, *Surf. Sci.* **2006**, *600*, 2528.
315. T. Schalow, B. Brandt, M. Laurin, S. Schauermann, J. Libuda, H.-J. Freund, *J. Catal.* **2006**, *242*, 58.
316. J. Middeke, R.-P. Blum, M. Hafemeister, H. Niehus, *Surf. Sci.* **2005**, *587*, 219.
317. D. E. Starr, F. M. T. Mendes, J. Middeke, R. P. Blum, H. Niehus, D. Lahav, S. Guimond, A. Uhl, T. Kluener, M. Schmal, *Surf. Sci.* **2005**, *599*, 14.
318. L. Xie, D. Wang, C. Zhong, X. Guo, T. Ushikubo, K. Wada, *Surf. Sci.* **1994**, *320*, 62.
319. T. Ushikubo, Y. Koike, K. Wada, L. Xie, D. Wang, X. Guo, *Catal. Today* **1996**, *28*, 59.
320. F. Höbel, A. Bandara, G. Rupprechter, H.-J. Freund, *Surf. Sci.* **2006**, *600*, 963.
321. K. T. Queeney, D. A. Chen, C. M. Friend, *J. Am. Chem. Soc.* **1997**, *119*, 6945.
322. D. A. Chen, C. M. Friend, *J. Am. Chem. Soc.* **1998**, *120*, 5017.
323. C. M. Friend, K. T. Queeney, D. A. Chen, *Appl. Surf. Sci.* **1999**, *142*, 99.
324. K. T. Queeney, C. M. Friend, *J. Phys. Chem. B* **2000**, *104*, 409.
325. I. Kretzschmar, J. A. Levinson, C. M. Friend, *J. Am. Chem. Soc.* **2000**, *122*, 12395.
326. L. J. Deiner, S. L. Wilcke, C. M. Friend, F. C. Nart, *Surf. Sci.* **2001**, *477*, L301.
327. K. T. Queeney, C. M. Friend, *Surf. Sci.* **1998**, *414*, L957.
328. K. T. Queeney, S. Pang, C. M. Friend, *J. Chem. Phys.* **1998**, *109*, 8058.
329. F. C. Nart, C. M. Friend, *J. Phys. Chem. B* **2001**, *105*, 2773.
330. I. N. Remediakis, E. Kaxiras, M. Chen, C. M. Friend, *J. Chem. Phys.* **2003**, *118*, 6046.
331. M. M. Biener, J. Biener, R. Schalek, C. M. Friend, *J. Chem. Phys.* **2004**, *121*, 12010.
332. M. M. Biener, C. M. Friend, *Surf. Sci.* **2004**, *559*, L173.
333. S. Guimond, Y. Romanyshyn, H. Kuhlenbeck, H. Freund, H. Cavalleri, K. Hermann, private communication.
334. C. Hardacre, G. M. Roe, R. M. Lambert, *Surf. Sci.* **1995**, *326*, 1.
335. K.-D. Schierbaum, *Surf. Sci.* **1998**, *399*, 29.
336. A. Siokou, R. M. Nix, *J. Phys. Chem. B* **1999**, *103*, 6984.
337. D. R. Mullins, P. V. Radulovic, S. H. Overbury, *Surf. Sci.* **1999**, *429*, 186.
338. W. Xiao, Q. Guo, E. G. Wang, *Chem. Phys. Lett.* **2003**, *368*, 527.
339. S. Eck, C. Castellarin-Cudia, S. Surnev, M. G. Ramsey, F. P. Netzer, *Surf. Sci.* **2002**, *520*, 173.
340. C. Xu, W. S. Oh, Q. Guo, D. W. Goodman, *J. Vac. Sci. Technol., A* **1996**, *14*, 1395.
341. C. Xu, W. S. Oh, D. W. Goodman, *J. Phys. Chem. B* **2000**, *104*, 10310.
342. M. Frank, K. Wolter, N. Magg, M. Heemeier, R. Kuhnemuth, M. Bäumer, H.-J. Freund, *Surf. Sci.* **2001**, *492*, 270.
343. J. Libuda, I. Meusel, J. Hartmann, H.-J. Freund, *Rev. Sci. Instrum.* **2000**, *71*, 4395.